J. Fluid Mech. (1995), *vol.* 285, *pp.* 265–301

Breaking of standing internal gravity waves through two-dimensional instabilities

By PASCALE BOURUET-AUBERTOT, J. SOMMERIA AND C. STAQUET

Laboratoire de Physique (URA 1325 CNRS), Ecole Normale Supérieure de Lyon, 46 allée d'Italie, 69364 Lyon Cedex 07, France

(Received 14 March and in revised form 12 September 1994)

The evolution of an internal gravity wave is investigated by direct numerical computations. We consider the case of a standing wave confined in a bounded (square) domain, a case which can be directly compared with laboratory experiments. A pseudo-spectral method with symmetries is used. We are interested in the inertial dynamics occurring in the limit of large Reynolds numbers, so a fairly high spatial resolution is used (129^2 or 257^2), but the computations are limited to a two-dimensional vertical plane.

We observe that breaking eventually occurs, whatever the wave amplitude: the energy begins to decrease after a given time because of irreversible transfers of energy towards the dissipative scales. The life time of the coherent wave, before energy dissipation, is found to be proportional to the inverse of the amplitude squared, and we explain this law by a simple theoretical model. The wave breaking itself is preceded by a slow transfer of energy to secondary waves by a mechanism of resonant interactions, and we compare the results with the classical theory of this phenomenon: good agreement is obtained for moderate amplitudes. The nature of the events leading to wave breaking depends on the wave frequency (i.e. on the direction of the wave vector); most of the analysis is restricted to the case of fairly high frequencies.

The maximum growth rate of the inviscid wave instability occurs in the limit of high wavenumbers. We observe that a well-organized secondary plane wave packet is excited. Its frequency is half the frequency of the primary wave, corresponding to an excitation by a parametric instability. The mechanism of selection of this remarkable structure, in the limit of small viscosities, is discussed. Once this secondary wave packet has reached a high amplitude, density overturning occurs, as well as unstable shear layers, leading to a rapid transfer of energy towards dissipative scales. Therefore the condition of strong wave steepness leading to wave breaking is locally attained by the development of a single small-scale parametric instability, rather than a cascade of wave interactions. This fact may be important for modelling the dynamics of an internal wave field.

1. Introduction

We here characterize wave breaking of an initially smooth wave field as the occurrence of energy dissipation in the limit of small viscosity, due to energy transfers towards dissipative scales. In the case of internal gravity waves, breaking also results

in irreversible vertical mixing of matter. This is therefore an important mechanism of vertical heat transfer and chemical transport in stably stratified media like the oceans or the atmosphere (e.g. Muller *et al.* 1986).

Breaking of interfacial gravity waves is observed when the amplitude becomes so large that local overturning occurs. The heavy fluid is then over lighter fluid, and a mechanism of Rayleigh–Taylor (convective) instability quickly leads to the loss of regularity and turbulence. Such a convective instability also occurs in the case of internal waves in a continuously stratified fluid, but a mechanism of shear instability can also lead to loss of regularity for similar wave amplitudes. Both mechanisms are encountered in the ocean: examples are given by Kunze, Williams & Briscoe (1990) for the former and by Orlanski & Bryan (1969) for the latter. Evidence of these two kinds of instabilities is also provided by laboratory experiments (e.g. Thorpe 1968; McEwan 1971; Orlanski 1972; Taylor 1992).

The occurrence of breaking is not limited to internal waves with very steep initial isodensity lines. For internal gravity waves of moderate amplitude, the breaking event itself is preceded by a slower phase of wave steepening. For instance, a propagating wave in a mean sheared medium progressively steepens and breaks near critical layers, where the propagating velocity with respect to the medium vanishes (e.g. Winters & D'Asaro 1989; Winters & Riley 1992). For standing waves considered here, this process cannot occur, but a mechanism of resonant interactions between different modes can transfer energy to smaller wavelengths. It results in a progressive increase of the local slope of the isodensity lines, eventually leading to breaking. Such standing waves correspond to the case of a confined domain, e.g. laboratory tanks. A periodic primary wave is then forced by a paddle (McEwan 1971; Orlanski 1972) or by parametric instability (McEwan & Robinson 1975; Thorpe 1994*c*; Benielli & Sommeria 1994). Breaking is indeed commonly observed in such experiments. In some other experimental conditions, with lower forcing amplitude, the secondary wave is stabilized by viscous effects, so that the nonlinear transfers between a limited set of modes can be studied in isolation, and found in good agreement with weakly nonlinear expansions (McEwan, Mander & Smith 1972). However, the succession of events leading to the wave breaking itself are difficult to analyse precisely in laboratory experiments.

Therefore direct numerical simulations can be very useful to analyse these mechanisms and compare them with theoretical models. During the initial stage (i.e. before wave breaking), Orlanski & Ross (1973) found a very good agreement between experiments, numerical results and analytic solution (up to second order in amplitude). After the onset of wave breaking however, comparisons with experiments show some differences, though a good qualitative agreement is obtained in particle trajectories. In fact these differences are the results of both a low resolution (32 grid points in the horizontal direction, 120 in the vertical direction) and the limited accuracy of the finite differences method. These results are also very sensitive to subgrid-scale modelling. Consequently, the turbulent regime was poorly described numerically, as underlined by Orlanski (1972). Subsequently, extensive two-dimensional numerical simulations were performed by Orlanski & Cerasoli (1980) (with a resolution of 51×61). The existence of a possible statistically stationary state through wave–wave interactions was addressed, and the energy transfers in the presence of a background random wave field were studied.

The mechanisms of wave breaking itself were not analysed in these previous numerical studies. This is the aim of the present paper: we start with a simple standing wave and study the succession of instabilities that lead to wave breaking.

Progress in computer technology, and the use of a precise pseudo-spectral method, allow much higher resolution than in previous works. The spatial organization of the growing perturbation leading to wave breaking can be clearly analysed, without significant smoothing by viscous effects. Furthermore, the theoretical interpretation of the initial instability in terms of resonant wave interactions is only possible for small wave amplitude, but breaking then occurs after many periods of the primary wave. Therefore it is also necessary to have a long time of integration, and three-dimensional computations with appropriate spatial resolution would be prohibitively long. We have thus chosen to restrict the problem to two-dimensional calculations in the vertical plane. Actual wave breaking clearly involves three-dimensional mechanisms, corresponding to a local convective instability in regions of overturned isodensity lines (e.g. Thorpe 1994*b*). However, the time of breaking and rate of energy loss for the primary wave must be controlled by the slowest mechanism in the succession of instabilities. In the case of an initial wave of moderate amplitude, the slowest process is the primary instability by resonant interaction, which can be two-dimensional with appropriate choice of experimental conditions (as for instance in McEwan 1983). Comparisons with laboratory experiments (see § 4) indicate that our two-dimensional model indeed captures much of the dynamics of a real system. Furthermore, turbulent regimes with buoyancy forces can be surprisingly well approached by a two-dimensional computation, as shown in the case of Rayleigh–Bénard convection (DeLuca *et al.* 1990; Christie & Domaradzki 1992; Bartoloni *et al.* 1993). Indeed energy transfers towards small scales are not forbidden by the local vorticity conservation, unlike in two-dimensional unstratified turbulence (e.g. Kraichnan & Montgomery 1980).

We briefly present the numerical model in the next section. In § 3, the initial regime is described: a standing internal wave with finite amplitude. The loss of coherence and subsequent breaking of this wave is described in § 4. In § 5, the first wave instability is interpreted in the framework of the theory of resonant interactions. In § 6, a predictive model for the breaking of high-frequency standing waves, using the idea of local parametric instability, is compared to the numerical results.

2. Numerical model

We solve the two-dimensional Navier–Stokes equations in the Boussinesq approximation, using a pseudo-spectral method (Canuto *et al.* 1988): the spatial derivatives are computed in Fourier space while the nonlinear terms are computed in physical space. The domain is a square in a vertical plane; in order to model the boundary conditions of laboratory experiments, normal velocities at the walls are set to zero. This is compatible with a pseudo-spectral method if symmetry boundary conditions are introduced. The normal velocity component is an odd function of the normal coordinate at each boundary, so that it vanishes there. The symmetries of the equations imply that the tangential velocity component is an even function of the normal coordinate (therefore its normal derivative vanishes: this is a free slip condition). The (reduced) density fluctuations ρ' have the same parity as the vertical velocity component. These symmetry properties allow the use of Fourier transforms, involving only sines or cosines, to compute spatial derivatives (e.g. Brachet *et al.* 1988). The computation of the nonlinear terms in physical space generates aliasing errors which are eliminated by a standard truncation method. Integration in time is performed using an explicit third-order Adams–Bashforth scheme and the diffusion terms are

calculated explicitly (Canuto *et al.* 1988, p. 204). Resolution is 129^2, with a few test runs at 257^2.

We use Cartesian coordinates (x, y), with vertical coordinate y directed upwards. A vertically displaced fluid particle oscillates with the buoyancy (Brunt–Väisälä) frequency N, defined by

$$N^2 = -\frac{g}{\rho_0}\frac{\mathrm{d}\bar{\rho}}{\mathrm{d}y},$$

where g is the acceleration due to gravity, ρ_0 is the density of a hydrostatic reference state and $\bar{\rho}(y)$ is the mean density profile. We assume that N is constant, so that $\bar{\rho}$ is linearly decreasing with the vertical coordinate y and does not vary with time. In the Boussinesq approximation, this basic density profile plus the superimposed density fluctuations ρ^*, stay close to the mean density ρ_0: $\bar{\rho}(y) + \rho^*(x, y, t) \approx \rho_0$ at any time. The condition of incompressibility is assumed, and taken into account by introducing a stream function ψ, related to the two velocity components u_x and u_y by

$$u_x = \partial_y \psi, \quad u_y = -\partial_x \psi.$$

We solve the Boussinesq equations in terms of the vorticity $-\Delta\psi$ and the reduced density fluctuations $\rho' = (g/\rho_0)\rho^*$:

$$\partial_t \Delta\psi + J(\Delta\psi, \psi) = \partial_x \rho' + \nu(-1)^{n+1}\Delta^{n+1}\psi, \tag{2.1}$$

$$\partial_t \rho' + J(\rho', \psi) = -N^2 \partial_x \psi + \frac{\nu}{Pr}(-1)^{n+1}\Delta^n \rho', \tag{2.2}$$

where the nonlinear advective terms are written by means of the Jacobian J, and the Prandtl number Pr is taken equal to unity unless otherwise specified. The numerical computations are performed in a square of length π on each side, with a Brunt–Väisälä frequency $N = 1$, and time will be scaled by the Brunt–Väisälä period $T_{BV} = 2\pi/N$. Any corresponding physical situation can be represented by these calculations with appropriate choices of length and time units.

Dissipation is modelled either by an ordinary diffusion, using a Laplacian term ($n = 1$) or by a bilaplacian ($n = 2$), which better restricts the dissipation to the highest wave vectors. Before each run, viscosity is adjusted to get its minimum possible value for a given spatial resolution. If viscosity, or the density diffusion coefficient, is too low, spurious noise accumulates at the smallest resolved scales. We check that the smallest spatial scales are well resolved by computing the different terms of the evolution equation for the total energy, $E = \frac{1}{2}\int\int(\rho'^2/N^2 - \psi\Delta\psi)\,\mathrm{d}x\,\mathrm{d}y$:

$$E(t) = E(0) + \underbrace{\int_0^t -\nu(-1)^{n+1}\langle\psi\Delta^{n+1}\psi\rangle\,\mathrm{d}t}_{KE_{diss}} + \underbrace{\int_0^t \frac{\nu}{Pr}(-1)^{n+1}\left\langle\frac{\rho'\Delta^n\rho'}{N^2}\right\rangle\mathrm{d}t}_{PE_{diss}} \tag{2.3}$$

where KE_{diss} and PE_{diss} denote the dissipation of kinetic and potential energy, and $\langle\,\rangle$ refers to a spatial average over the numerical domain. We discard the equation results, and increase the viscosity, if (2.3) is not verified within a precision of at least 1%. The numerical parameters chosen for different initial conditions are indicated in tables 1 and 2.

In the specific case of a low-frequency mode, the flow has a much smaller scale along the vertical than along the horizontal direction, and it was useful to increase the vertical resolution in comparison with the horizontal one. For that purpose, we still use a square domain with a square numerical mesh, but in terms of a dilated vertical coordinate. We are then led to make corresponding changes in time scale and

Run	Mode	Range of amplitude, a	dt	Resolution
I1	(5,1)	[0.024, 0.056]	4×10^{-3}	129^2
I2	(1,1)	[0.08, 0.4]	4×10^{-3}	129^2
I3	(1,5)	[0.004, 0.016]	4×10^{-3}	129^2

TABLE 1. Initial conditions and numerical parameters: case of an inviscid fluid. The time steps are indicated in BV periods, the amplitude is dimensionless. In the case of a low-frequency mode, the vertical scale is expanded by a factor of 5.

Run	Mode	Amplitude: a	Dissipation	dt	Resolution
V1	(5,1)	0.072	$\Delta^2, \nu = 4 \times 10^{-7}$	3×10^{-3}	129^2
V2	(5,1)	0.02188	$\Delta^2, \nu = 4 \times 10^{-8}$	3×10^{-3}	129^2
V3	(5,1)	0.012	$\Delta^2, \nu = 4 \times 10^{-9}$	3×10^{-3}	129^2
V4	(5,1)	0.008	$\Delta^2, \nu = 4 \times 10^{-9}$	3×10^{-3}	129^2
V5	(1,1)	0.4	$\Delta^2, \nu = 2 \times 10^{-7}$	2×10^{-3}	257^2
V6	(1,1)	0.4	$\Delta^2, \nu = 4 \times 10^{-7}$	4×10^{-3}	129^2
V7	(1,1)	0.4	$\Delta^2, \nu = 8 \times 10^{-7}$	8×10^{-3}	65^2
V8	(1,1)	0.328	$\Delta^2, \nu = 4 \times 10^{-5}$	4×10^{-3}	129^2
V9	(1,1)	0.256	$\Delta, \nu = 3 \times 2.10^{-5}$	4×10^{-3}	129^2
V10	(1,1)	0.256	$\Delta^2, \nu = 4 \times 10^{-7}$	4×10^{-3}	129^2
V11	(1,1)	0.192	$\Delta^2, \nu = 4 \times 10^{-8}$	4×10^{-3}	129^2
V12	(1,1)	0.128	$\Delta^2, \nu = 2 \times 10^{-8}$	4×10^{-3}	129^2
V13	(1,1)	0.064	$\Delta^2, \nu = 4 \times 10^{-9}$	4×10^{-3}	129^2
V14	(1,5)	0.032	$\Delta^2, \nu = 2 \times 10^{-5}$	2×10^{-3}	257^2
V15	(1,5)	0.016	$\Delta^2, \nu = 2 \times 10^{-6}$	2×10^{-3}	257^2

TABLE 2. Initial conditions and numerical parameters: case of a viscous fluid. The time steps are indicated in BV periods, the amplitude and dissipation are dimensionless.

dynamical functions according to the following relationships:

$$\tilde{x} = k_x x, \ \tilde{y} = k_y y, \ \tilde{t} = t \cos\theta, \ \tilde{\psi} = (k_x k_y / \cos\theta)\psi, \ \tilde{\rho} = \rho' k_y, \tag{2.4}$$

where the dilation coefficients k_x and k_y are the horizontal and vertical components of the initial mode wave vector, and $\tan\theta = k_y/k_x$. We numerically solve the equations obtained by making these changes of variables in all the terms of (2.1) and (2.2), except the diffusive ones: we still keep the same form of the diffusive terms with the new variables. This procedure is equivalent to increasing the numerical resolution only in the vertical direction, and reducing the vertical diffusive term accordingly. The introduction of such an anisotropic diffusion should not have a significant effect because the dynamics is controlled by inertial effects, and it allows better resolution of the strong gradients which are mostly in the vertical direction.

3. The standing internal gravity wave

The aim of this study is to observe the evolution of a simple standing wave, until breaking occurs. It is therefore natural to choose an initial condition with an unperturbed density field, and the velocity field of a linear standing wave (normal mode), with stream function ψ and density ρ':

$$\psi(x, y) = a \ \sin(k_x x) \sin(k_y y), \ \rho'(x, y) = 0, \tag{3.1}$$

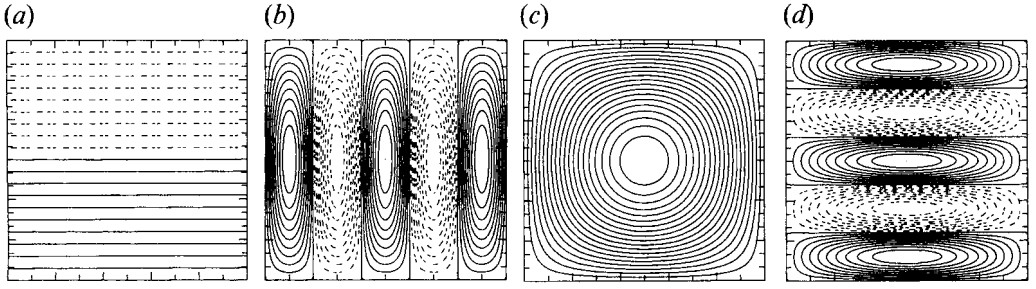

FIGURE 1. Different initial conditions, given by equation (3.1), for a standing wave. (*a*) total density field, (*b–d*) vorticity field (similar to the streamfunction), (*b*) $\boldsymbol{k} = (5,1)$, (*c*) $\boldsymbol{k} = (1,1)$, (*d*) $\boldsymbol{k} = (1,5)$.

represented in figure 1 for different choices of k_x, k_y. This velocity field will displace the isodensity lines (figure 2*a*), and the buoyancy restoring force will then reverse the velocity field, leading to periodic oscillations. The linear solution for this standing wave is

$$\left.\begin{aligned} \psi(x,y,t) &= a\,\sin(k_x x)\sin(k_y y)\cos(\omega t), \\ \rho'(x,y,t) &= -a\frac{k_x N^2}{\omega}\cos(k_x x)\sin(k_y y)\sin(\omega t). \end{aligned}\right\} \tag{3.2}$$

The frequency ω is given by the linear dispersion relationship

$$\omega = N\,|\cos\theta| = N\,|k_x/k| \tag{3.3}$$

where θ is the angle of the wavenumber vector with the horizontal direction (the frequency can also be defined as negative, with the same modulus); k is the modulus of the wavenumber vector. This standing wave can be seen as the superposition of four pairs of plane waves with frequencies $+\omega$ and $-\omega$, and wavenumber vectors $(k_x,k_y),(-k_x,k_y),(k_x,-k_y),(-k_x,-k_y)$. For simplicity, we will refer to this solution as the mode $\boldsymbol{k} = (k_x,k_y)$, and remember that the mode structure is unchanged by reversing any of the wavenumber vector components, and its oscillation is unchanged by reversing the frequency.

While a single plane wave is an exact solution of the nonlinear equations (2.1) and (2.2) (in an unbounded domain), the standing wave (3.2) is only a solution of the linearized equations (the Jacobian vanishes in the hydrodynamic equation (2.1) but not in the density equation (2.2)). Therefore, the evolution of the initial condition (3.1) involves nonlinear interactions, and the actual solution will progressively depart from the linear approximation. The importance of the nonlinear effects may be estimated by the Froude number (see § 5.2)

$$Fr = \frac{U}{Nl},$$

where U is a typical velocity and l a typical length. If we choose $l = 1/k$ and the typical velocity $U = ka$, the Froude number is defined as

$$Fr = k^2 a/N.$$

In other words, the influence of nonlinear effects is estimated by comparing the typical wave vorticity to the Brunt–Väisälä frequency N (but $N = 1$ with our time unit). Another measure of the importance of nonlinear effects is the maximum slope h of the isodensity lines. The local slope is $-\partial_x\rho^*/(\partial_y\rho^* + \mathrm{d}\bar{\rho}/\mathrm{d}y)$. For a wave of low amplitude, $\partial_y\rho^*$ is neglectable and the slope reduces to $\partial_x\rho'/N^2$, and its maximum

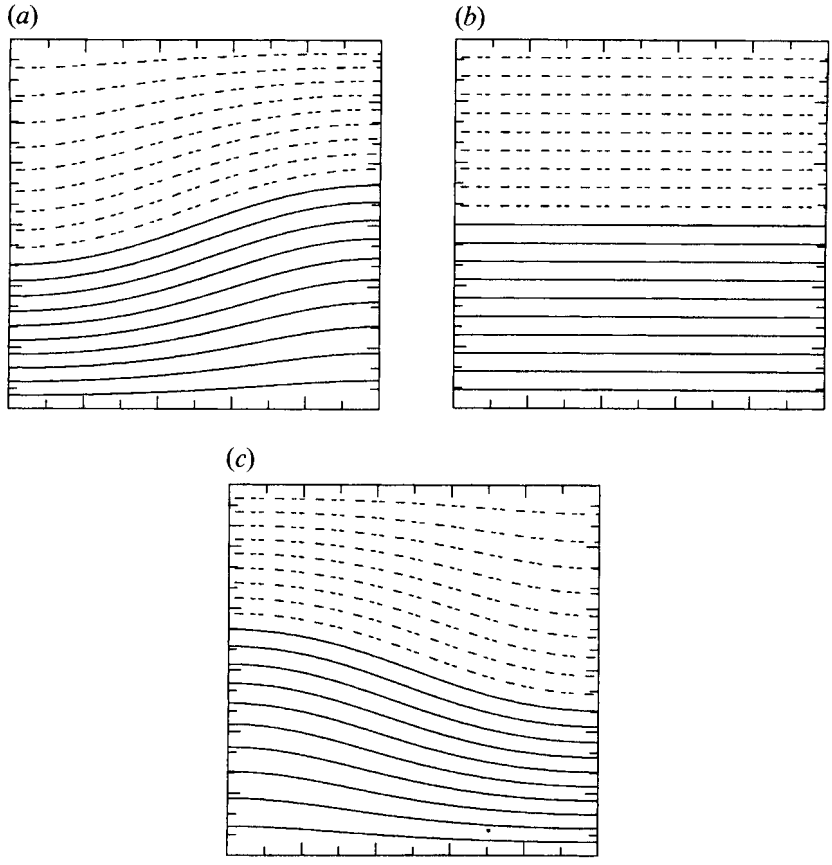

FIGURE 2. Total density fields after (*a*) one quarter, (*b*) half, (*c*) three quarters of the wave period (initial condition (3.1) with $\boldsymbol{k} = (1, 1)$ and $a = 0.256$, run V9).

value in the linear approximation (3.2) is

$$h = \frac{k_x^2 a}{\omega} = Fr \cos\theta.$$

This characterization of the nonlinear effects differs from the previous one in the angular dependency. The influence of θ on the nonlinear effects cannot be estimated by mere dimensional arguments, but it requires a complete theory.

We shall see that whatever the wave amplitude, the coherence will be progressively lost and wave breaking eventually occur (but this will require more time as the amplitude is lower). However there also exists a branch of particular solutions which remain a periodic wave: this is the continuation of a linear standing wave as the amplitude is increased. Its structure can be obtained by an expansion in the amplitude a (Thorpe 1968):

$$\psi(x, y, t) = a \sin(k_x x) \sin(k_y y) \cos(\omega' t) + a^3 \frac{k^2 k_y^2}{128} \sin(k_x x) \left[\frac{\sin(3k_y y) \cos(\omega' t)}{N^2 - \omega^2} - \frac{\sin(3k_y y) \cos(3\omega' t)}{10N^2 - 9\omega^2} + \frac{\sin(k_y y) \cos(3\omega' t)}{N^2} \right], \quad (3.4a)$$

$$\rho(x,y,t) = -aN^2\frac{k_x}{\omega'}\cos(k_x x)\sin(k_y y)\sin(\omega' t) - a^2\frac{k^2 k_y}{8}\sin(2k_y y)(1-\cos(2\omega' t))$$
$$+a^3 N\frac{k{k_y}^2}{128}\cos(k_x x)\left[\frac{8k^2}{N^2}\sin(k_y y)\sin(\omega' t) + \frac{3(k_x^2+9k_y^2)}{10N^2-9\omega^2}\sin(3k_y y)\sin(3\omega' t)\right.$$
$$\left. -\frac{k_x^2+9k_y^2}{N^2-\omega^2}\sin(3k_y y)\sin(\omega' t) - \frac{3k^2}{N^2}\sin(k_y y)\sin(3\omega' t)\right] \qquad (3.4b)$$

(notations have been translated from Thorpe 1968, and a misprint in his expression for ρ has been corrected).

Thorpe has also calculated the variation of the frequency ω' with the amplitude and obtained the following expression, up to fourth order (Thorpe, private communication):

$$\omega' = \omega\left(1 - \frac{{k_x}^2{k_y}^2}{32\omega^2}a^2 + \frac{{k_x}^4{k_y}^4(3k_x^4+37k_x^2k_y^2+67k_y^4)}{64^2\,k_y^4(k_x^2+10k_y^2)\omega^4}a^4\right) + o(a^5) \qquad (3.5)$$

(the same relation has been also obtained by Sekerzh-Zen'covich (1983), up to second order, from the Boussinesq equations in Lagrangian coordinates).

Our initial condition (3.1) fits with the expansion of Thorpe at $t = 0$ up to second order, so we expect to obtain a nearly periodic oscillation with frequency close to (3.5). The contribution of the primary wave (3.1) in the Fourier decomposition is indeed periodic to within an excellent approximation (figure 3*a*). The period is measured as the time interval between two successive zeros of this main Fourier component, and this is quite constant (within 10^{-4} in relative variation) during the few first oscillations (after this initial regime, the breaking process develops, and the calculation diverges in the absence of viscosity). While the main Fourier component is periodic, harmonics are excited with a complex behaviour, for instance the mode (1,3) represented in figure 3(*b*). These harmonics can be made periodic by adjusting their initial amplitude (figure 3*c*), as discussed in § 5.2. The initial condition is then the expansion for the nonlinear periodic wave (3.4) at $t = 0$ instead of the pure primary wave (3.1).

The relative difference between the measured period and the linear period (3.3) is plotted versus the square of the wave amplitude in figure 3(*d–f*). This difference is close to the linear law predicted by the term of order a^2 in (3.5) (dashed straight line). Some discrepancy appears at the highest amplitudes, especially for the mode (5,1), and the agreement is improved by taking into account the term in a^4 in (3.5) (dashed curve). However the numerical result is between these two curves, suggesting that the series (3.5) is oscillating with fairly slow convergence. This remaining difference is however very small ($\sim 10^{-4}$ in relative value) and is close to the limit of the numerical precision. The difference would be better measured at higher wave amplitudes, but breaking then occurs during the first period of motion. Therefore the fourth-order expansion (3.5) already gives an excellent prediction of the primary wave period for practical purposes. This is true even when we choose the initial condition (3.1), instead of the nonlinear wave (3.4).

4. Loss of coherence and breaking of the standing wave

A remarkably organized perturbation progressively develops upon the standing wave, and its structure is best represented by the vorticity field (figure 4). It is a

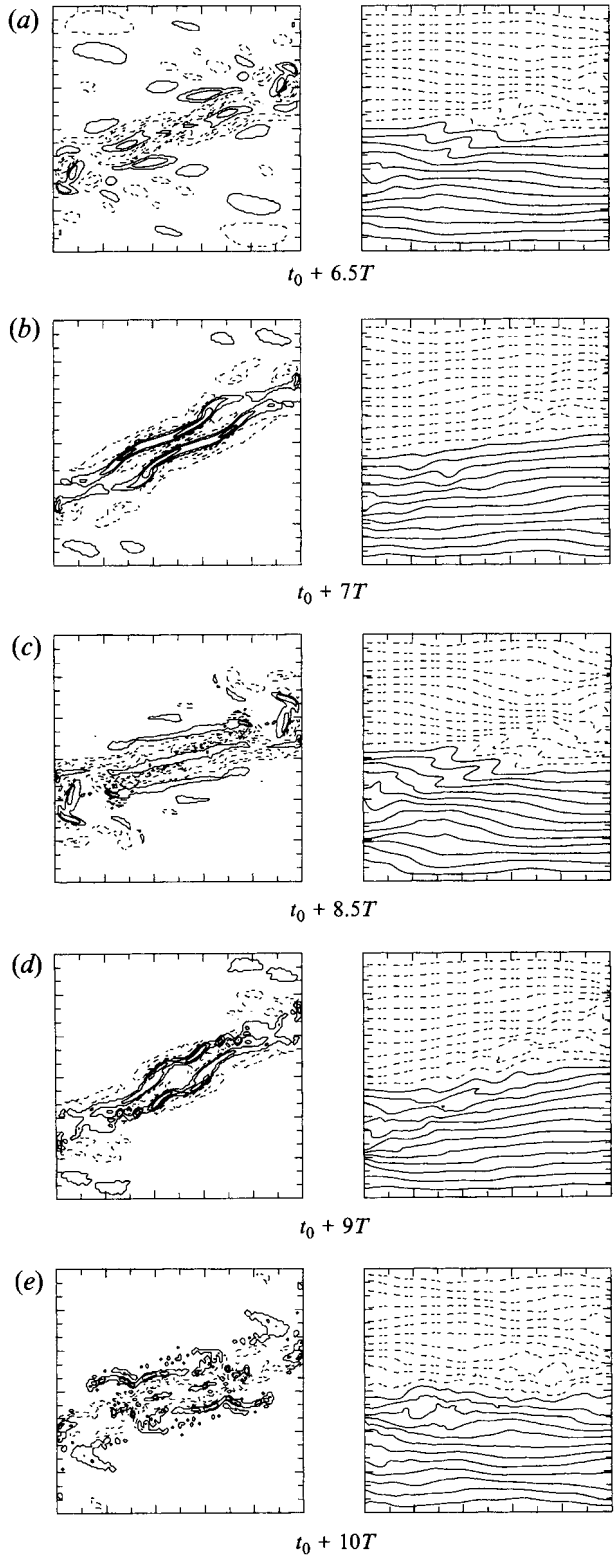

FIGURE 5. For caption see facing page.

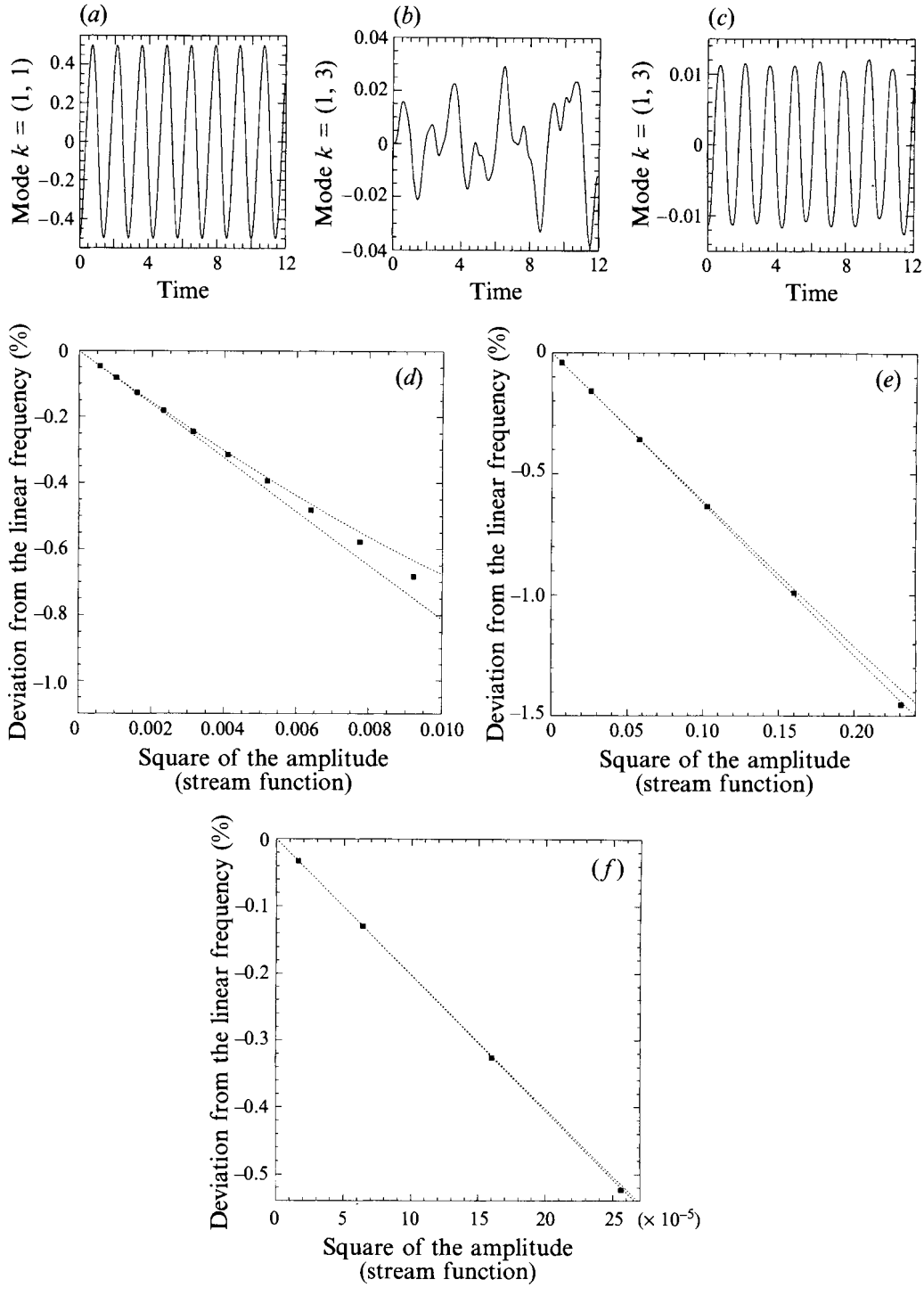

FIGURE 3. For caption see facing page

(figure 8*c*). This difference of behaviour can be related to the linear stability diagrams of the primary wave, as analysed in the next section.

5. The growth of subharmonic instabilities

5.1. *The general Floquet analysis*

The progressive departure from a purely periodic oscillation can be considered as an instability of the ideal nonlinear periodic standing wave. The small initial difference with this ideal wave is progressively amplified. A complete treatment of this problem would first require the determination of the ideal periodic wave with finite amplitude, whose fourth-order expansion is given by (3.4). Then, using such an ideal periodic wave as a basic state, the eigen modes and growth rates of the linear stability problem should be determined. Since the basic flow is periodic in time, the perturbation can be expanded on the basis of Floquet modes. Such a general analysis has been performed, using numerical methods, in the case of a plane travelling wave (Mied 1976; Drazin 1977; Klostermeyer 1982, 1983, 1990, 1991), but the extension to the present problem of standing waves remains to be done. However, the problem can be treated in the case of two important limiting cases. When the amplitude of the primary wave is small, the dynamics is controlled by resonant interactions and can be analysed by a low-order expansion in Froude number (§ 5.2). The instability of the pure standing wave then appears as a particular case of the more general theory of resonant interactions (which can be applied for any initial field of low amplitude). The other limiting case is the local parametric instability, when the perturbation is at small scale in comparison with the primary wave, as discussed in § 6.

5.2. *The dynamics of weakly interacting waves*

The dynamics of a wave field with low amplitude can be approximated by an expansion in terms of the Froude number, taken as a small parameter. This approach is quite general in wave theory and has been developed for surface waves by Phillips (1960, 1961), Hasselmann (1962*a*, *b*), and applied to progressive internal waves by Davis & Acrivos (1967). The calculations for standing internal gravity waves have been performed by Thorpe (1968), McEwan (1971) and McEwan *et al.* (1972). It is useful to briefly summarize these results here, before applying them to our computations. Since the interaction between waves is weak, each mode oscillates in first approximation with its frequency (3.3) given by the linear theory, but its phase and amplitude can slowly vary under the effects of wave interactions. The problem is formalized in terms of a multi-scale expansion (e.g. Bender & Orszag 1978), introducing a rapid time t_0 and a slow time t_1, and each field formally depends on these two times. The wave oscillates as a function of the rapid time t_0, and the

FIGURE 3. (*a*) Amplitude of the mode (1,1) for an initial condition (given by equation (3.1)) with $\boldsymbol{k} = (1,1)$. (*b*) Amplitude in the mode (1,3) for the same computation. (*c*) Amplitude in the mode (1,3) when the nonlinear wave (3.4) is introduced at $t = 0$ (times are indicated with the unit T_{BV}). (*d*) Relative deviation of the computed wave period with the linear period given by (3.3), versus the amplitude squared a^2; the theoretical results (3.5) are indicated by the straight dashed line (up to $o(a^2)$) and by the dashed curve (up to $o(a^4)$); the stream function (3.4) is introduced at $t = 0$ with $\boldsymbol{k} = (5,1)$ (runs I1); (*e*) same as (*d*) but $\boldsymbol{k} = (1,1)$ (runs I2); (*f*) same as (*d*) but $\boldsymbol{k} = (1,5)$ (runs I3).

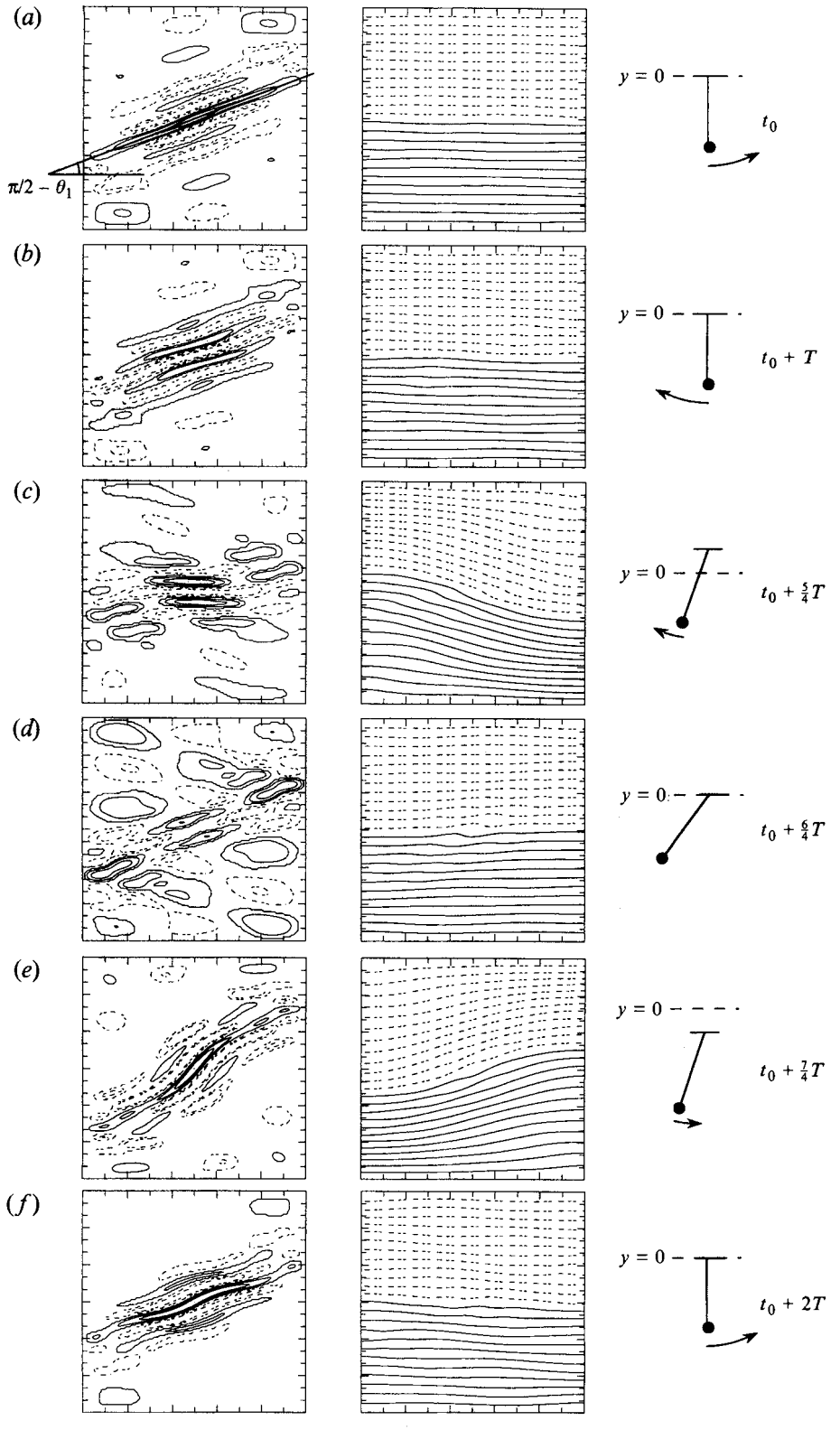

FIGURE 4. For caption see facing page

amplitude and phase of this oscillation depends on t_1. All time derivatives in (2.1) and (2.2) are then written as

$$\partial_t = \partial_{t_0} + Fr\,\partial_{t_1} \tag{5.1}$$

while the fields are expanded in Froude number

$$\left.\begin{aligned} \psi(t_0, t_1, ...) &= \psi_0(t_0, t_1, ...) + Fr\,\psi_1(t_0, t_1, ...) + ..., \\ \rho'(t_0, t_1, ...) &= \rho'_0(t_0, t_1, ...) + Fr\,\rho'_1(t_0, t_1, ...) + ... \end{aligned}\right\} \tag{5.2}$$

(at each next order in Froude number, a still slower time scale would have to be introduced).

Introducing this form of solution in the Boussinesq equations (2.1) and (2.2), we get at zero order in Fr, the linearized wave equation:

$$(\partial_{t_0}^2 \Delta + N^2 \partial_x^2)\,\psi_0 = 0, \quad \partial_{t_0}\rho'_0 = -N^2 \partial_x \psi_0. \tag{5.3}$$

The general zero-order solution corresponding to our boundary conditions is a superposition of linear standing waves (3.2). However, their amplitudes a_i and phases α_i depend in general on the slow time scale t_1:

$$\left.\begin{aligned} \psi_0(x, y, t_0, t_1) &= \sum_i a_i(t_1) \sin(k_{x_i} x) \sin(k_{y_i} y) \cos(\omega_i t_0 + \alpha_i(t_1)), \\ \rho'_0(x, y, t_0, t_1) &= -N^2 \sum_i \frac{k_{x_i}}{\omega_i} a_i(t_1) \cos(k_{x_i} x) \sin(k_{y_i} y) \sin(\omega_i t_0 + \alpha_i(t_1)), \end{aligned}\right\} \tag{5.4}$$

where the frequency ω_i is given by the dispersion relation (3.3).

Introducing the zero-order solution in (2.1) and (2.2), we get the first order equations

$$(\partial_{t_0}^2 \Delta + N^2 \partial_x^2)\,\psi_1 = -2\partial_{t_0}\partial_{t_1} \Delta\psi_0 - \partial_{t_0} J(\Delta\psi_0, \psi_0) - \partial_x J(\rho'_0, \psi_0), \tag{5.5}$$

$$\partial_{t_0}\rho'_1 = -N^2 \partial_x \psi_1 - J(\rho'_0, \psi_0) - \partial_{t_1}\rho'_0. \tag{5.6}$$

The quadratic nonlinear terms in the right-hand side of (5.5) are composed only of

---

FIGURE 4. Development of the secondary instability in the form of a plane wave packet (initial condition (3.1) with $\boldsymbol{k} = (1, 1)$ and $a = 0.256$, run V9): successive snap shots of the vorticity field (1st column) and the total density field (2nd column). For the vorticity fields, the contribution in the Fourier mode (1,1) has been removed in order to better visualize the perturbation itself (and the represented iso-values depend on the extrema, with solid lines for positive values and dashed lines for negative values). In the last column, the corresponding position of a pendulum (analogous to the secondary wave) is indicated for comparison: it is parametrically excited by the vertical oscillation around a fixed reference level (dashed line) of its support (the horizontal solid line), analogous to the primary wave. (*a*) $t = 60.4\ T_{BV}$(42.5 periods of the main wave have occurred since $t = 0$); (vorticity range [−0.20;0.36]). The deformation vanishes while the velocity (and vorticity) is extremal. The predicted inclination (6.2) of the perturbation wave crests $\theta_1 = 20.7°$ is indicated. (*b*) $t = 61.8\ T_{BV}$, after one period T of the main wave, the phase of the secondary wave has been reversed (vorticity range: [−0.42;0.29]) (*c*) $t = 62.1\ T_{BV}$, 1/4 period later, the pattern has been rocked by the main wave and reaches its minimum slope. (vorticity range:[−0.30;0.32]). The analogous pendulum rises with its support at the upper position (its rising motion then benefits from a lower apparent gravity). (*d*) $t = 62.5\ T_{BV}$, the secondary wave is close to extremal in deformation, and has weak vorticity so that the resonant triad (2,6) (3,7) is visible. (vorticity range [−0.24;0.27]) (*e*) $t = 62.8\ T_{BV}$, the structure has been rocked in the opposit direction, reaching its maximum slope (isovalues of the vorticity:[−0.29;0.56]). The analogous pendulum is going downward with its support at its lower position (its motion then benefits from the highest apparent gravity). (*f*) $t = 63.2\ T_{BV}$, the structure of (*a*) is recovered (with the development of a secondary perturbation) (vorticity range [−0.39;0.54]).

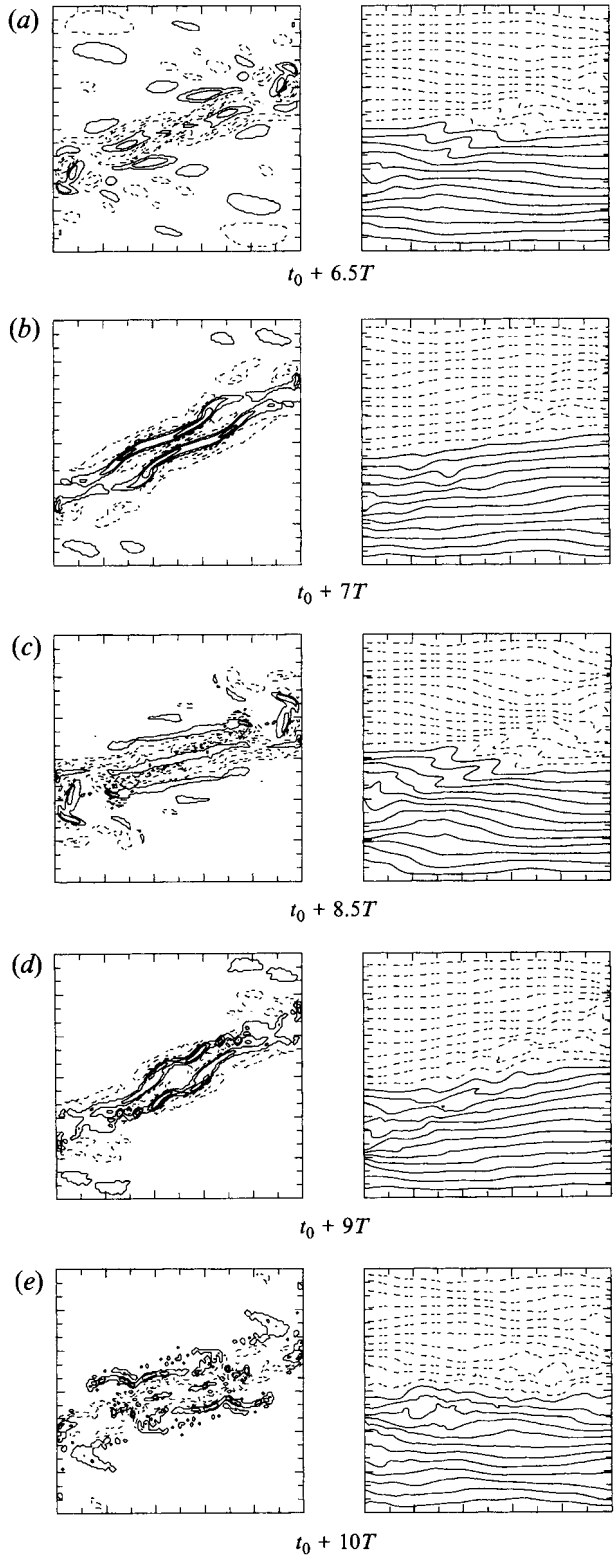

FIGURE 5. For caption see facing page.

Fourier modes with wavenumber vectors obtained by sums and differences of the wavenumber vector components excited at zero order. This is the condition of spatial resonance for nonlinear interactions:

$$\boldsymbol{k}_1 + \boldsymbol{k}_2 + \boldsymbol{k}_3 = 0 \tag{5.7}$$

where $\boldsymbol{k}_2$ and $\boldsymbol{k}_3$ are any pair of wavenumber vectors defining the modes excited at zero order (any resonant relation with a minus signs can be transformed into such a sum relation by inverting the corresponding wavenumber vector components, which does not change the mode, as previously noted). Each of the quadratic terms in the right-hand side of (5.5) oscillates with frequencies which are sums and differences of the natural frequencies of the zero-order modes $\boldsymbol{k}_2$ and $\boldsymbol{k}_3$ in the triad. The amplitude of the first order perturbation, projected on the mode $\boldsymbol{k}_1$, thus behaves like an oscillator, excited at frequencies $\omega_2 \pm \omega_3$ by the right-hand terms. If this excitation is not resonant, i.e. if it does not involve the natural frequency ω_1 (given by (3.3)) of the oscillator, a permanent oscillation is obtained at the exciting frequency. The general solution for the first order perturbation, projected on the mode $\boldsymbol{k}_1$, is a superposition of this permanent solution, and a transient solution at the natural frequency ω_1. In the absence of dissipation, this 'transient' solution persists in fact forever, and its amplitude is determined by the initial condition. Therefore the forced oscillation at frequencies $\omega_2 \pm \omega_3$ coexists with the natural frequency ω_1, except for particular initial conditions. In this case of non-resonant interaction, the slow time scale is not needed: the nonlinear perturbation is controlled by the zero-order waves on a rapid time scale.

However if the frequency of a right-hand nonlinear term corresponds to its natural frequency ω_1, the first-order perturbation is excited without bound. This is the condition of temporal resonance, which occurs in addition to the condition of spatial resonance (5.7):

$$\omega_1 + \omega_2 + \omega_3 = 0 \tag{5.8}$$

(notice that each mode can be represented both by positive and negative frequencies, so this relation covers all possible sign combinations). The perturbation projected on mode $\boldsymbol{k}_1$ then reaches the zero-order level, and the validity of the expansion would then break down, except if the term $2\partial_{t_0}\partial_{t_1}\Delta\psi_0$ introduced by the slow time scale exactly balances the nonlinear resonant term. This condition leads to an evolution equation for the zero-order amplitude a_1 and phase α_1:

$$k_1^2 \dot{a}_1 = a_2 a_3 S\omega_1 \cos(\varphi),\ k_1^2 a_1 \dot{\alpha}_1 = -S\omega_1 a_2 a_3 \sin(\varphi), \tag{5.9}$$

where $\varphi = \alpha_3 + \alpha_1 + \alpha_2$, and S is the interaction coefficient, given by McEwan *et al.* (1972) (but there is a mistake by a factor of two in that paper)

$$S = \frac{N^2}{16\omega_1\omega_2\omega_3}(k_{x_r}\omega_s - k_{x_s}\omega_r)(k_{x_s}k_{y_r} - k_{x_r}k_{y_s})\left(\frac{k_{x_1}}{\omega_1} + \frac{k_{x_2}}{\omega_2} + \frac{k_{x_3}}{\omega_3}\right) \tag{5.10}$$

FIGURE 5. Snapshots showing the breaking of the wave of figure 4, by vorticity fields (1st column) and total density isovalues (2nd column). (*a*) $t = 69.5\ T_{BV}$ (49 periods of the main wave have occurred since $t = 0$): the density is extremal and iso-lines first overhang, while vorticity perturbation is weak. (*b*) $t = 70.2\ T_{BV}$: vorticity is extremal and the strips are still weakly deformed. (*c*) $t = 72.3 T_{BV}$: density perturbation is again extremal and overhangs more than in (*a*). (*d*) $t = 73.0\ T_{BV}$: the vorticity strips begin to break into chains of vortices. (*e*) $t = 73.7\ T_{BV}$: the secondary wave is now strongly disrupted.

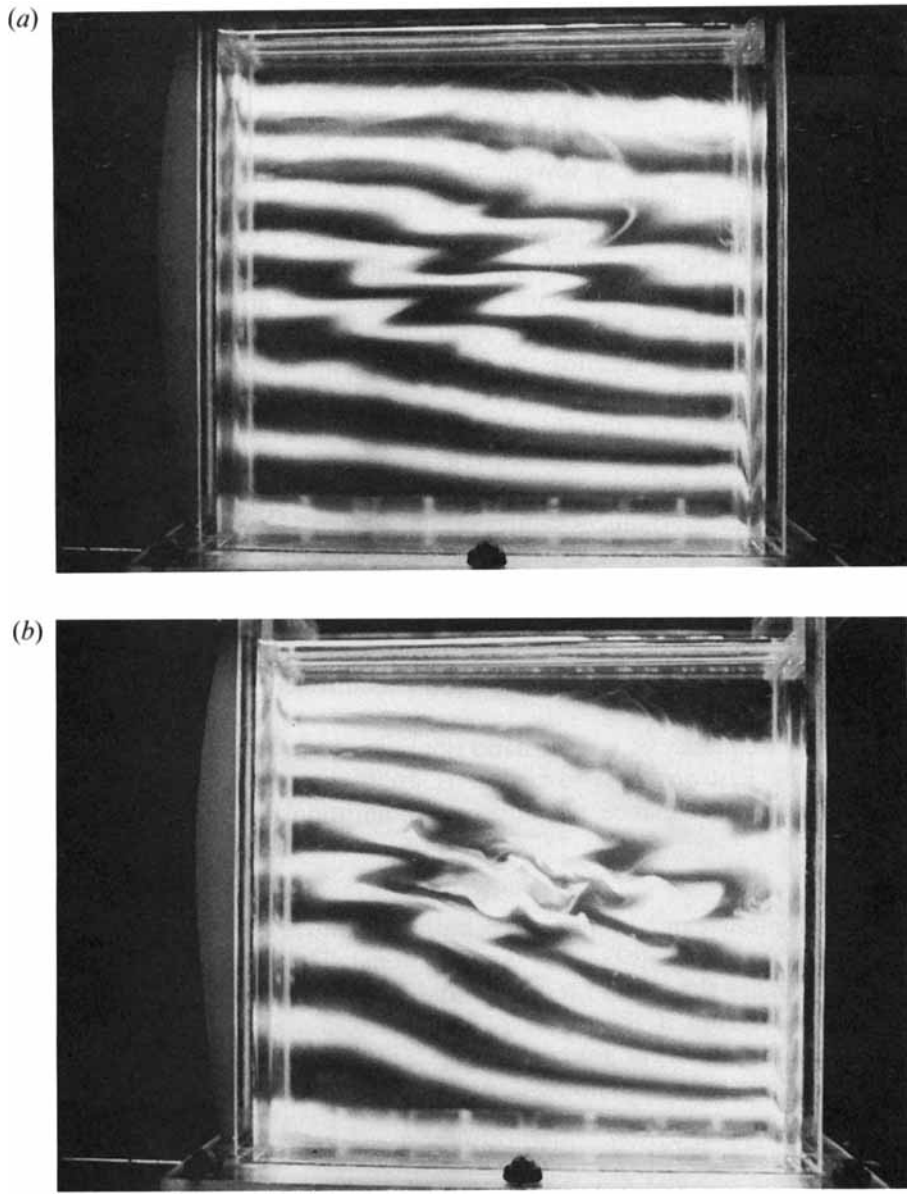

FIGURE 6. Laboratory experiments (from Benielli & Sommeria 1994). The displacement is visualized by bands of dye which are initially horizontal, made fluorescent by a vertical sheet of laser light. The tank has a square vertical cross-section (25 cm × 25 cm) and breadth 9 cm, and the developing primary wave has essentially a two-dimensional structure in the vertical plane. This primary wave is excited by the parametric instability due the vertical oscillation of the supporting plateform. We see here the development of the secondary instability (*a*) leading a few periods later to wave breaking (*b*). This mechanism is quite similar to the simulations shown in figures 4 and 5. However, note that during the later turbulent stage three-dimensional processes are involved: convective rolls are observed along the third dimension.

where r and s stand for any pair among the indices 1,2,3. The evolution equation for the modes 2 and 3 contains a similar term, obtained by circular permutation. In the case of a single resonant triad, a closed dynamical system is thus obtained. Its structure is best displayed in terms of the complex amplitudes $A_i = a_i \exp(j\omega_i t + \alpha_i)$, and their complex conjugate A_i^*:

$$k_1^2 \dot{A}_1 = A_2^* A_3^* S\omega_1, \; k_2^2 \dot{A}_2 = A_1^* A_3^* S\omega_2, \; k_3^2 \dot{A}_3 = A_1^* A_2^* S\omega_3. \tag{5.11}$$

Since the interaction coefficient S scales like k^4, the triad interaction depends on the vorticities of the interacting modes (and on the angular positions of their wave vectors). This is in agreement with the dimensional analysis of § 3, stating that the nonlinear effects depend on the typical vorticity or Froude number. If some random noise is added to the pure standing wave, it will contain modes forming a resonant triad with the primary wave, and the interaction equation (5.11) can lead to an exponential amplification of these initially small perturbations. This is the classical mechanism of wave instability by resonant interactions, which is summarized in § 5.3.

However there is generally no significant random noise added to the numerical computation, and the initiation of such a resonant instability must be discussed. If the initial state is a pure mode of the form (3.1), the only spatially resonant triad is (k_x, k_y),$(-k_x, k_y)$,$(0, -2k_y)$. This triad also satisfies the condition (5.8) for a temporally resonant triad, but according to (5.11), the amplitude of the mode $(0, 2k_y)$ is stationary, since its frequency is zero. The amplitude of the mode $(0, 2k_y)$ is then given as a second-order perturbation: it is the solution of (5.6) which vanishes at $t = 0$ (since the initial density profile is unperturbed). This perturbation in density, given by (3.4) as the term in a^2, is always associated with the standing wave, and has no associated velocity: it is in fact a perturbation of the vertical density profile. The same procedure can be applied at next order, and it gives an interaction equation (5.11) involving the amplitude of the primary wave and the density perturbation in the mode $(0, 2k_y)$. For this particular triad, a constant derivative for the phase α is obtained, and this is equivalent to the nonlinear correction in frequency (3.5).

At this third order, there is also a non-resonant excitation of the mode (k_x, k_y), obtained as the sum of $(0, 2k_y)$ and $(k_x, -k_y)$, at frequency 3ω, and of the mode $(k_x, 3k_y)$ (sum of $(0, 2k_y)$ and (k_x, k_y)) at frequencies 3ω and ω (the amplitudes of these modes are given by (3.4) as the terms in a^3). Such forced modes have frequencies which are always multiples of the primary frequency ω, so that the resulting wave is purely periodic in time. However, the values of these harmonics at the initial time is imposed. Therefore, if the initial condition is not carefully adjusted, transient oscillations at the natural frequency of the mode $(k_x, 3k_y)$ must be superposed upon the primary wave, and the resulting evolution is not periodic, as seen on figure 3(*b*). Many other modes are excited during the first oscillations by non-resonant interactions at higher orders, and in general each of these modes oscillates at its natural frequency, in addition to the frequency of the nonlinear harmonic forcing. All the corresponding natural frequencies must then appear, except for a very specific adjustment of the initial condition, defining the nonlinear periodic wave. These oscillations can therefore initiate the instability of the primary wave by resonant interactions.

5.3. *Application to the instability of the standing wave*

The instability of a primary wave is described by (5.11), in which the complex amplitudes A_1 and A_2 are supposed to be very small in comparison with the third amplitude, denoted A, corresponding to the primary wave. Therefore A is constant

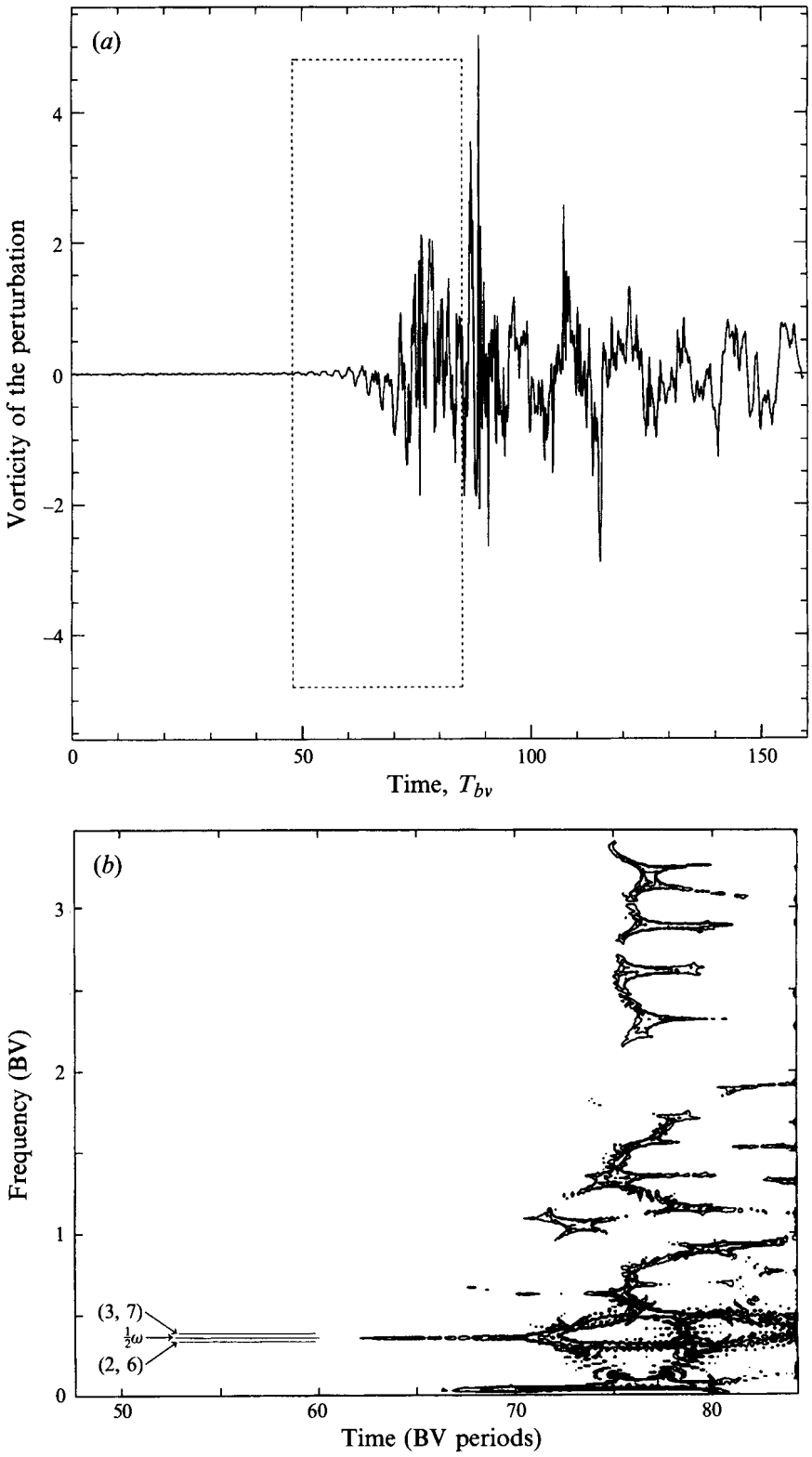

FIGURE 7. For caption see facing page.

(and assumed to be real by an appropriate definition of the phase) and A_1 and A_2 are solutions of the linear system

$$k_1^2 \dot{A}_1 = A_2^* A^* S\omega_1, \; k_2^2 \dot{A}_2 = A_1^* A^* S\omega_2. \tag{5.12}$$

The stability properties are obtained by diagonalizing this system. If ω_1 and ω_2 have opposite sign, the eigen values are purely imaginary, and the perturbation does not grow. By contrast, if ω_1 and ω_2 have the same sign, we obtain a solution with exponential growth rate

$$s = \frac{S}{k_1 k_2} a(\omega_1 \omega_2)^{1/2} \tag{5.13}$$

such that $A_2 = \sigma(k_1/k_2)(\omega_2/\omega_1)^{1/2} A_1^*$; and also a decaying solution at rate $-s$, such that $A_2 = -\sigma(k_1/k_2)(\omega_2/\omega_1)^{1/2} A_1^*$ (σ is the sign of S). It is probable that one of the two modes 1 or 2 is dominantly excited by the non-resonant interactions during the first periods of motion (i.e. at $t_1 = 0$ but $t_0 \neq 0$), so that the resulting mode amplitudes are the sum and difference of these two eigen modes: one amplitude grows like cosh (st) and the other one like sinh(st).

The condition of instability that ω_1 and ω_2 have the same sign is equivalent to the statement that the primary wave can only feed secondary waves with smaller frequencies (in absolute values). Indeed, if for instance ω is positive, the two secondary frequencies must both be negative, in order to satisfy (5.8), so that the sum of their absolute values must be equal to ω, and each of these absolute values is therefore smaller than ω. This remarkable condition results from quite general physical principles, as shown by Hasselmann (1967) and Davis & Acrivos (1967).

The interacting triads can be represented by the extremity of the vector $\boldsymbol{k}_1$ in the plane, $\boldsymbol{k}_2$ being then determined by the condition of spatial resonance (5.7). The additional condition of temporal resonance defines lines on the plane, which are represented on figure 10 for three cases of the primary mode. The condition of quantization of the wave vectors due to the boundary conditions still restricts the possibilities for resonant triads: each wave-vector component must be an integer. Furthermore, since the initial perturbations at the origin of the instability are excited by non-resonant interactions at different orders, their constitutive modes must have wavenumber-vector components which are integer multiples of the primary wave components. This condition of quantization is more restrictive than the mere effect of the boundary conditions (except in the particular case of the primary mode (1,1)).

The line defining the resonant triads in figure 10 only exceptionally reaches the points defined by the quantization. However the condition (5.8) of temporal resonance need not be exact, but only verified within a precision of order Fr, such that the triad

---

FIGURE 7. (*a*) Vorticity at the central point of the domain (initial condition (3.1) with $\vec{k} = (1,1)$ and $a = 0.256$, run V9). The contribution of the Fourier mode (1,1) of the primary wave has been removed in order to better analyse the perturbation itself. (*b*) Corresponding time spectrogram during the interval delimited by a rectangle in (*a*). A Fourier transform is calculated over a shifting analysing (Gaussian) window. The width of this window is $18.4 T_{BV}$. Isovalues (6, 24dB) of the modulus of the transform are represented in the plane time–frequency (time is in T_{BV} and frequency in T_{BV}^{-1}). The method of reallocation of Auger & Flandrin (1994) has been used in order to improve the resolution in the time–frequency plane. The frequency half the primary wave ($0.352\ T_{BV}^{-1}$), and the linear frequencies of the secondary modes (2,6), $0.316 T_{BV}^{-1}$, and (3,7), $0.394 T_{BV}^{-1}$ are shown for comparison.

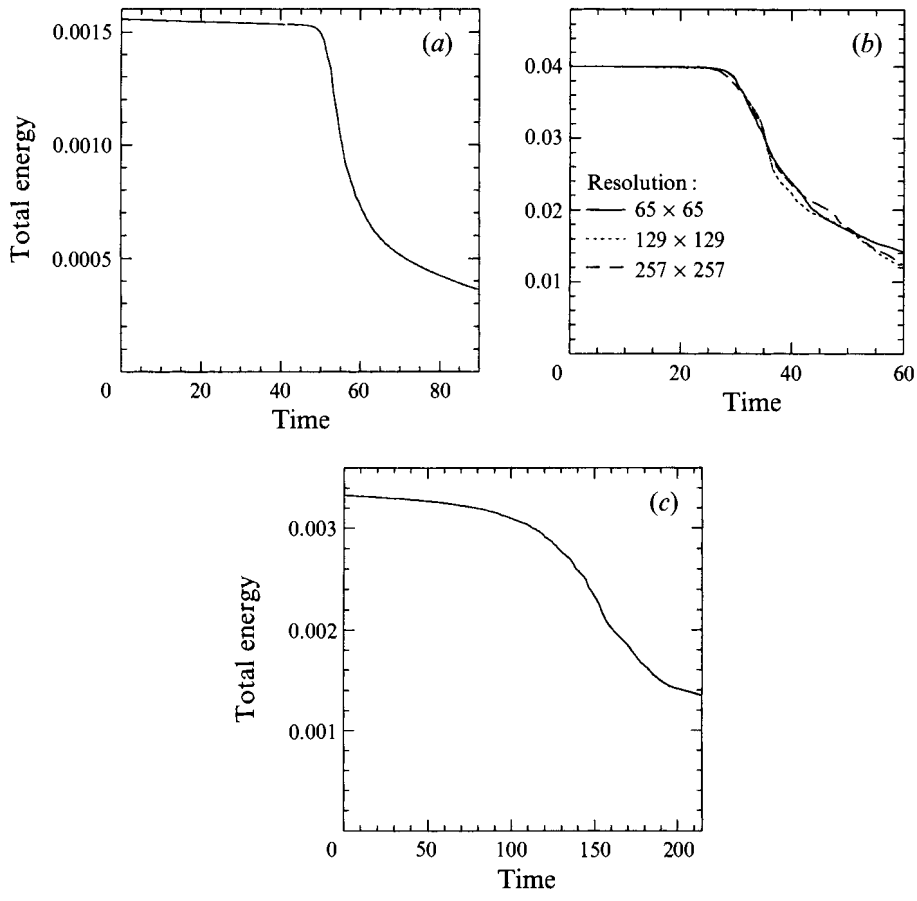

FIGURE 8. Decay of the total energy versus time (expressed in T_{BV} periods) for a standing wave with initial condition (3.1) (*a*) primary wave $\boldsymbol{k} = (5, 1)$, $a = 0.0219$ (runV2) (*b*) primary wave $\boldsymbol{k} = (1, 1)$, $a = 0.40$, three computations, with different resolutions $65^2, 129^2, 257^2$ and different coefficients of biharmonic dissipation (runs V5–7 of table 2), give very similar results. (*c*) primary wave $\boldsymbol{k} = (1, 5)$, $a = 0.032$ (runV14)

remains in a coherent phase relationship during the process of instability growth. Therefore, the lines of figure 10 represent the centre of an instability band whose width increases in proportion to the primary wave amplitude. The width of these instability bands is obtained by McEwan & Plumb (1977) in the case of progressive waves, by analysing the influence of a small detuning on the resonant interactions. Along the asymptotic branches reaching high values of k, the problem is simplified, since the instability becomes a parametric instability, and the classical results for the Mathieu equation apply. In this case, the secondary waves can be excited when their frequency is in the range $[\omega/2 - s, \omega/2 + s]$, which does indeed scale in Fr. Since the condition of temporal resonance involves angles of the wavenumber vector with respect to the horizontal, the width of the resonance bands increases in proportion to the wavenumber (for a given primary wave amplitude). Along the asymptotic branches reaching high values of k, the quantization condition is no longer effective when the band width is greater than unity (corresponding to wavenumbers k scaling like Fr^{-1}).

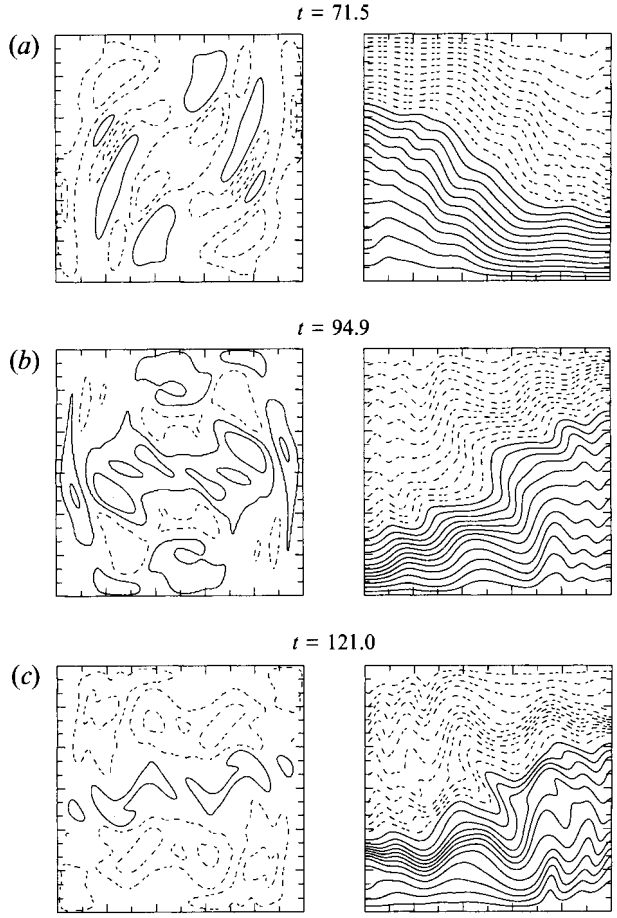

FIGURE 9. Snapshots showing the evolution of a standing wave (3.1) with low frequency leading to overhanging iso-density lines (mode $\boldsymbol{k} = (1,5)$ with $a = 0.032$, runV14). The vertical scale is magnified 5 times by means of the change of variables (2.4). (*a*) $t = 71.5\ T_{BV}$ (range of vorticity: [−0.41;0.39]); (*b*) $t = 94.9\ T_{BV}$ (range of vorticity: [−0.88;0.77]); (*c*) $t = 121.0\ T_{BV}$ (range of vorticity: [−0.87;0.50])

Along the lines defining temporal resonance, the theoretical growth rate is calculated by (5.13) and (5.10), and represented on figure 11 as a function of the angle θ_1 (figure 11*a*, *c*, *e*). We check that the growth rate vanishes for θ_1 smaller than the angle θ of the primary mode, in agreement with the general condition of instability that each secondary frequency must be lower than the primary one. An alternative representation is in terms of the wave number k_1 (figure 11*b*, *d*, *f*). We observe an important qualitative difference between the high frequency modes ((5,1) and (1,1)) and the low-frequency mode (1,5): in the latter case the branch C is more developed, and contains the modes with maximum growth rate, while for high-frequency primary waves, the maximum growth rate is obtained along an asymptotic branch (denoted A) with high wavenumbers (this property has been also obtained for progressive plane waves of finite amplitude by Mied 1976 and Klostermeyer 1982). The presence of a fine-scale structure of instability, with the vorticity bands of figure 4, is related to this remarkable linear stability property. Therefore most of our study is devoted to the case of a high-frequency primary wave. The asymptotic

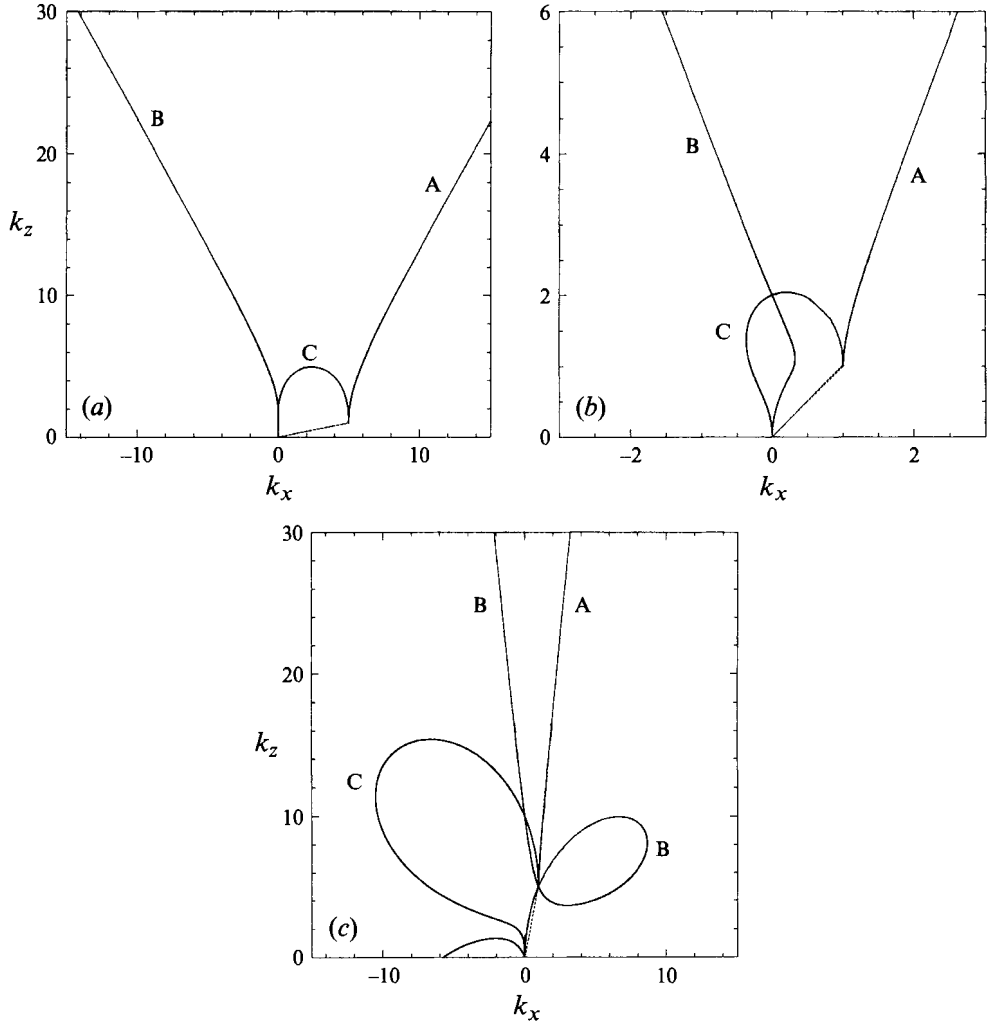

FIGURE 10. Diagram of the possible resonant triads involving a given primary wave. The triads, satisfying both (5.7) and (5.8), are represented by the extremity of the vector $-\boldsymbol{k}_1$ in the (x, y)-plane, defining 3 portions of curve denoted A, B, C. The primary wavenumber vector $\boldsymbol{k}_3$ is represented by the dashed segment (*a*) $\boldsymbol{k} = (5, 1)$, (*b*) $\boldsymbol{k} = (1, 1)$, (*c*) $\boldsymbol{k} = (1, 5)$.

frequency along branch A is just half the primary frequency, and the growth rate becomes

$$s = \frac{k^2 a \cos^2\theta}{32}(\tan\theta_1 - \tan\theta)[1 + \cos(\theta_1 - \theta)] \tag{5.14}$$

where $\cos\theta_1 = \frac{1}{2}\cos\theta$. In this limit of high wavenumber vector, the condition of quantization becomes irrelevant, as noted above, and we then understand why the instability always develops at high wavenumbers in the corresponding numerical computations (figure 4). In the presence of viscosity, the modes at high wavenumbers would be more strongly damped, resulting in a maximum growth rate at an optimum wavenumber (that increases as the viscosity gets smaller). This would select the scale of the perturbation that eventually dominates.

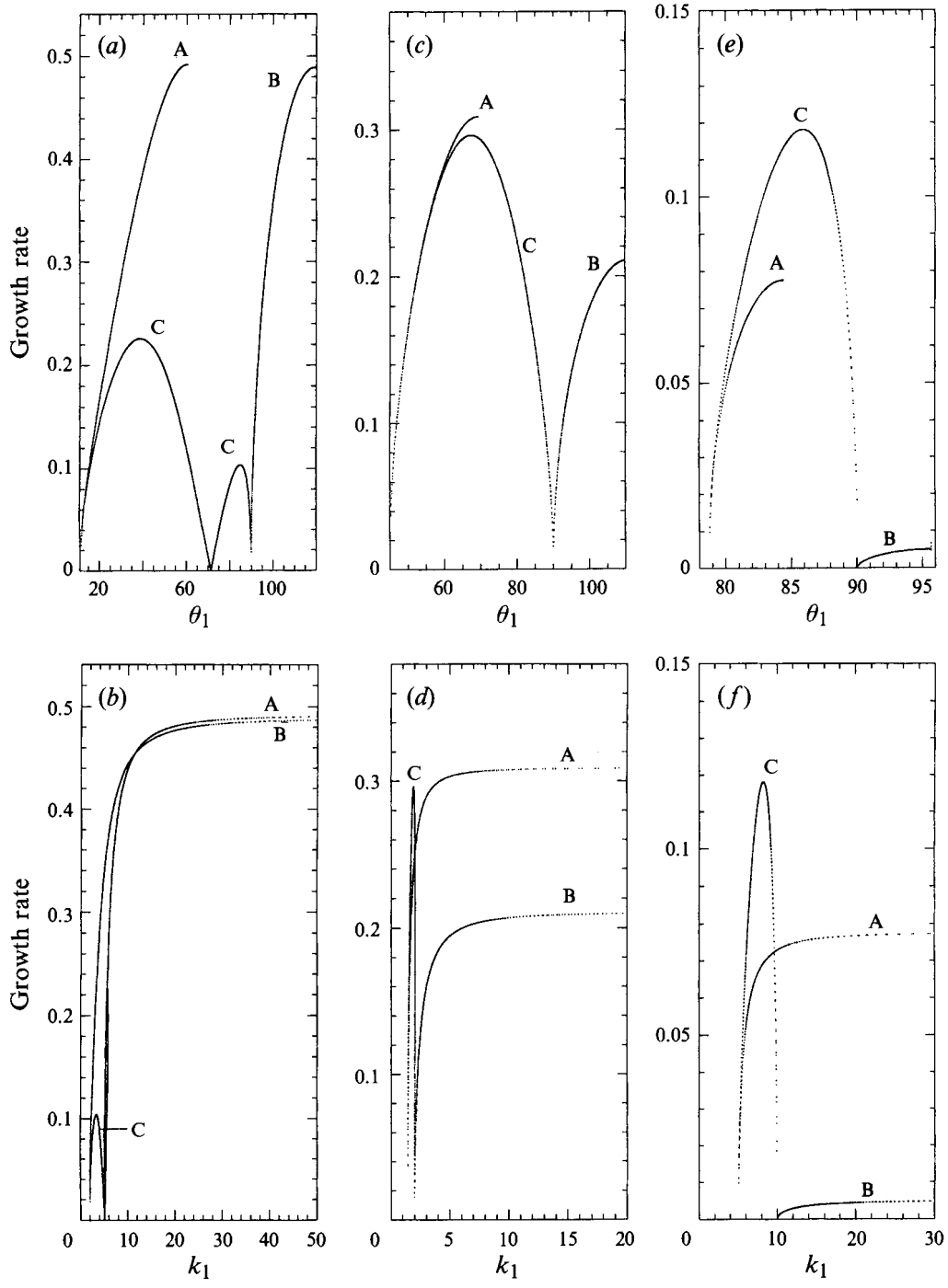

FIGURE 11. Normalized growth rate sT_{BV}/Fr from (5.13) for the resonant triads belonging to the branches A, B, C of figure 10. (*a*),(*c*),(*e*): growth rate versus angle θ_1 of the wavenumber vector $\boldsymbol{k}_1$ with horizontal for mode (5, 1), (1, 1) and (1, 5) respectively. (*b*),(*d*),(*f*): growth rate versus $|\boldsymbol{k}_1|$ for the same three modes.

In the limiting case of very weak viscosities that we consider in the wave breaking problem, there is however a wide range of wavenumbers with nearly identical growth rates. In that case, the initial condition plays an important role in this selection, since the different modes are initiated with widely different amplitudes. In the linear phase of the instability, the amplitude of each mode i grows like

$$A_i(t_1) = A_i(0)\exp(s_i t_1).$$

The initial amplitude $A_i(0)$ depends in a complex way on the initial condition, through the non-resonant interactions during the first periods of the wave. Each mode i is excited at some order n in the Froude number expansion, and its amplitude $A_i(0)$ then scales like Fr^n. The order n depends on the details of the wave structure, but it is roughly proportional to the ratio k_i/k of the wavenumber over the primary wavenumber: indeed the wavenumber vector k_i is reached by a sum of the primary wave vector components involving typically k_i/k terms. Therefore the resonant triad involving the lowest wavenumber k_i will generally dominate the initial instability growth, if its growth rate is close to the asymptotic limit. When the typical vorticity of the secondary modes becomes of the same order as the vorticity of the primary wave, the interactions between the secondary modes become important. Tertiary modes can be excited by new triad interactions, and a very complex nonlinear behaviour could be expected. However, the numerical computations reveal that the excited secondary modes tend to organize into a coherent plane wave packet (figure 4), inside which the nonlinear interactions are strongly reduced. Such a structure is best described in terms of a local mechanism of instability, following the ideas of McEwan & Robinson (1975), to be discussed in § 6. Yet the formalism of resonant interactions provides excellent predictions of the instability growth rate, as shown in the next section.

5.4. *Numerical test of the theory of resonant interactions*

We have performed systematic computations for the two high-frequency modes (5,1) and (1,1) with different amplitudes. The exploration of the low-frequency case (mode (1,5)) is still preliminary, and will be discussed separately at the end of the section. In order to test the theoretical predictions, we have computed the evolution of the total energy in each Fourier mode, and selected the modes that reach a given threshold during the instability growth (to stay in the wave regime before the breaking itself, we stop this procedure when the maximum absolute value of vorticity reaches the value 1). Resonant triads are indeed detected among these most excited modes, represented in figure 12, and they belong to the branch with highest growth rate (denoted A on figure 10). For the primary wave (5, 1), and the two secondary modes (10, 14) and (5, 13), the condition of resonance (5.7) is satisfied within 4% of the primary wave frequency and it is satisfied within 2% for the secondary modes (15, 23) and (10, 22). For the primary mode (1, 1), and the secondary modes (2, 6) and (3, 7), the condition of resonance is satisfied within a precision of 0.4%. These modes are indeed among the most excited ones, but modes of higher wavenumber on the instability branch A are also excited, as expected. We also notice the presence of many temporally non-resonant modes. These are entrained by the nonlinear interactions with the unstable modes and cooperate to form the organized bands shown in figure 4.

Indeed all the secondary modes grow with the same rate, found to be in good agreement with the theory for the asymptotic branch A. The time evolution of the energy of a few selected modes is plotted on figure 13, with logarithmic ordinate, and the theoretical growth rate (5.14) is indicated for comparison. The initial energy ($< 10^{-30}$) comes only from the numerical noise, but rises to a larger value set by

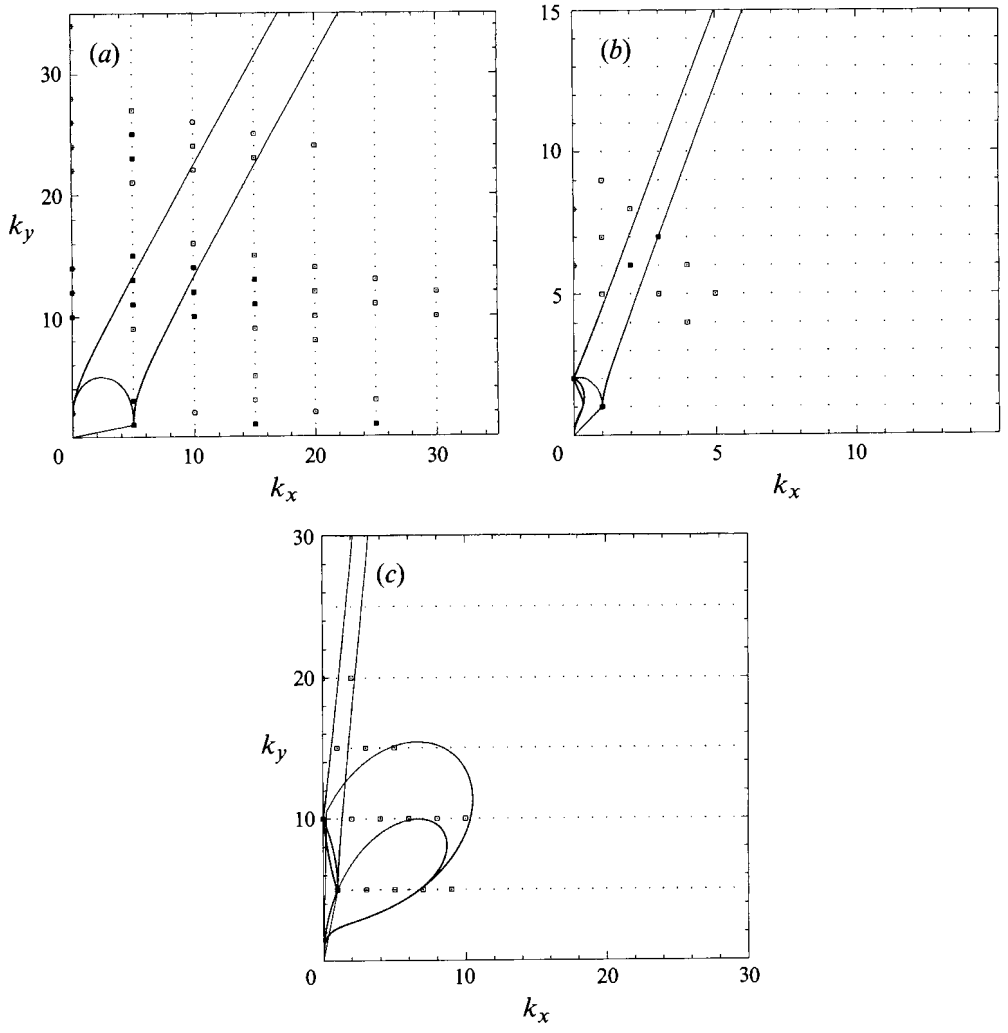

FIGURE 12. Diagram of the most excited Fourier modes during the instability growth. The modes whose energy exceeds a threshold 1/100 and 1/1000 of the initial wave energy are indicated respectively by the two different symbols ■, □. The lines of the resonant interactions from figure 10 are indicated for comparison (note that a symmetry through the k_y axis has been used). (*a*) Primary wave (5,1), $a = 0.0219$ (run V2). (*b*) Primary wave (1,1), $a = 0.256$ (run V9). (*c*) Primary wave (1,5), $a = 0.032$ (run V14)

the non-resonant interactions during the first period of oscillation (we have removed the first period from the curves to restrain their vertical scale). After a period of adjustment, the resonant component of the oscillation, at the mode natural frequency, dominates the non-resonant part, and the instability develops exponentially†. In fact the growth is strongly modulated by interactions with other growing modes, as clearly

† This period of adjustment depends on the particular choice of the initial condition: the initial non-resonant excitation of these modes at their natural frequency is probably very weak in comparison with excitation of the same spatial mode at harmonic frequencies, and only the former can initiate the resonant interaction. The adjustment period is reduced when we initiate the calculation with a pure density perturbation instead of a pure velocity perturbation (2.4).

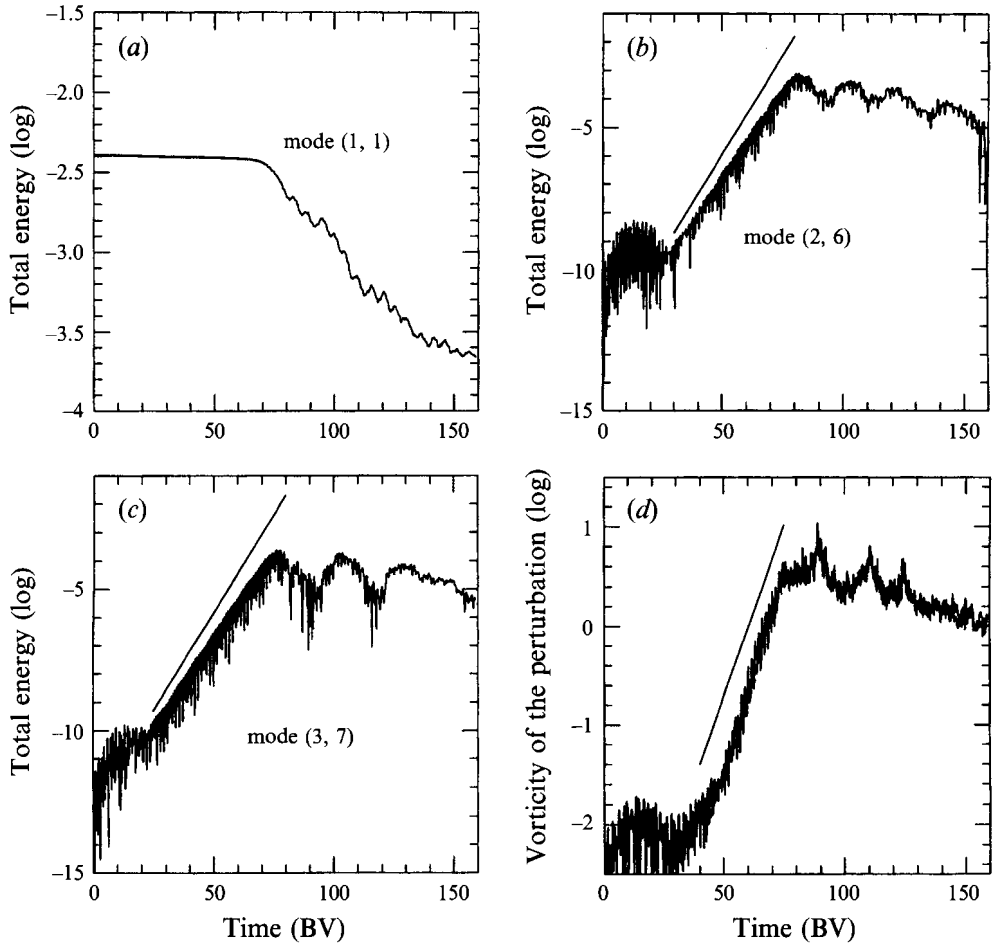

FIGURE 13. Growth of the primary wave instability, initial mode (1, 1) with $a = 0.256$ (run V9). (*a*) Evolution of the energy in the primary mode. (*b*, *c*) Growth of the energy in the two secondary modes (2,6) and (3,7) forming an isolated resonant triad with (1,1). (*d*) Growth of the vorticity extremum. The slopes obtained from the theory of resonant interactions (5.14) are indicated.

seen for the modes (2,6) and (3,7). In spite of such strong nonlinear interactions, which are also responsible for the phase locking that maintains the shape of the growing wave packet, it is remarkable that the growth rate is still well predicted by the theory. The measured growth rate is plotted versus the primary wave amplitude in figure 14. For the mode (1,1), it increases linearly with amplitude a_3, except for the highest Froude number 0.8. Since the resonant interaction theory is supposedly restricted to low Froude number, this agreement is unexpected. A similar behaviour is obtained for the mode (5,1), the growth rate being slightly lower than the theory for moderate primary wave amplitudes.

For the low-frequency primary wave (1,5), the situation is more complex, since modes belonging both to branch A and branch C are excited. According to the theory of resonant interactions at first order, the branch C contains the modes with maximum growth rate (see figures 11*e* and 11*f*), but in a fairly narrow region, here forbidden by the condition of quantization. The resonant triad of branch C

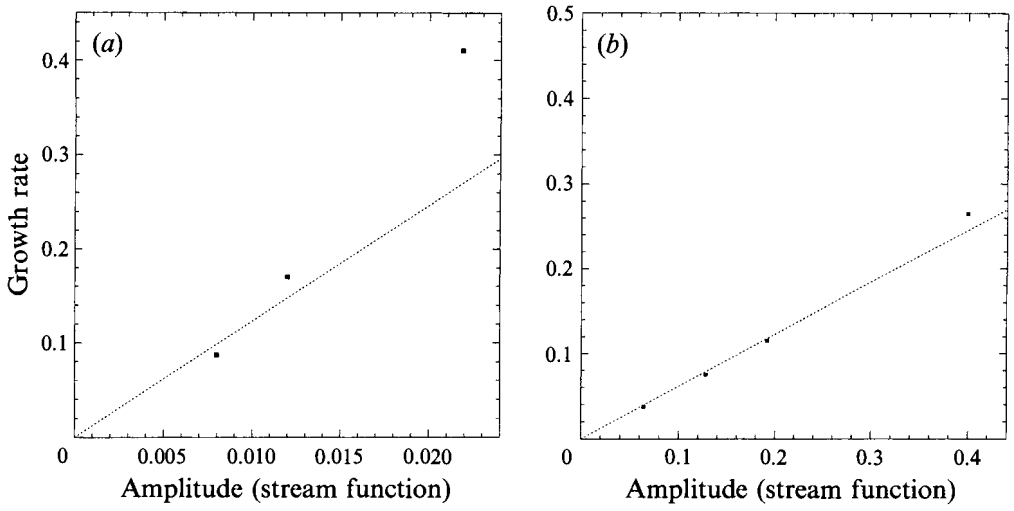

FIGURE 14. Numerical growth rate of the primary instability versus the amplitude of the primary wave, compared with the theory of resonant interaction (5.14) (dashed lines). (*a*) wave $k = (5, 1)$ (runs V1–4). (b) wave $k = (1, 1)$ (runs V5–13)

detected in figure 12(*c*) ((8,10),(7,5),(1,5)) is in another part of this branch, and transfers energy from the primary wave towards modes of higher frequencies. This is forbidden as a general result of the theory of resonant interactions at first order, but the growth of these modes of higher frequencies probably results from higher-order resonant interactions because the primary wave has a fairly high amplitude. Therefore the theory of resonant interactions accounts for the different behaviour of the low-frequency modes, but a thorough study of this latter case remains to be done.

6. A model for wave breaking

6.1. *Local parametric instability due to the primary wave rocking motion*

When the most rapidly growing perturbations are at large wavenumbers, it makes sense to consider that the perturbation is a local plane wave which is distorted and transported by the primary wave motion. Such an analysis has been performed by McEwan & Robinson (1975), who have found that the rocking motion of the primary wave around the node in displacement can amplify the perturbation by a mechanism of parametric instability. A perturbing wave of the form

$$\rho' = R(t)\cos(q_X X + q_Y Y) \tag{6.1}$$

is considered in the rocking frame of reference (X, Y). The natural frequency of this perturbing wave depends on the angle θ_q of its wave vector $\vec{q}$ with the horizontal; and this frequency is therefore modulated by the rocking motion, at the frequency of the primary wave. Such a modulation amplifies the perturbing wave when its natural frequency is close to half the frequency ω of the primary wave. This is obtained when the mean angle $\langle\theta_q\rangle$ satisfies

$$\langle\theta_q\rangle = \theta_1, \ \cos\theta_1 = \tfrac{1}{2}\cos\theta. \tag{6.2}$$

This mean angle is the actual angle of the perturbing wavenumber vector when the density perturbation of the primary wave vanishes, and the angle of the wave crests

with the horizontal is then the complementary of θ_1. For instance, in the case of the primary mode (1,1), the predicted angle is 20.7°, in good agreement with the mean angle of the vorticity strips in the numerical computation, as shown in figure 4(*a*).

Amplification of the secondary wave occurs with a well-defined phase, in analogy with a pendulum suspended at a vertically oscillating point, as illustrated on figure 4. The apparent gravity is modulated in the frame of reference attached to the suspension point. When the apparent gravity is higher than average, the pendulum goes downward (figure 4*e*), and when it is lower, the pendulum goes upward (figure 4*c*), so that the oscillating part of the apparent gravity always brings energy to the pendulum. In the same way, the displaced fluid particles in the secondary wave come toward equilibrium when the slope of their motion is maximum, and go away from equilibrium when the slope is minimum, so this oscillating motion receives net energy from the tilting motion of the primary wave. Since the phase of this secondary perturbation does not depend on the position, it must be indeed a standing wave (6.1), instead of a progressive wave. In other words, it can be considered as the sum of two progressive plane waves moving in opposite directions.

In the limit of small primary wave amplitude, and in the absence of diffusive effects, the perturbation $R(t)$ satisfies a Mathieu equation (obtained from McEwan & Robinson 1975):

$$\ddot{R} + N^2 \cos^2\theta_q [1 - \tan\theta_q \, \alpha_M \cos(\omega t)] R = 0 \tag{6.3}$$

where α_M is the angular amplitude of the rocking motion of the primary wave: α_M is equal to the maximum slope h of the deformed isodensity lines, defined in § 3. The resulting growth rate of the perturbation is then

$$s_q = \tfrac{1}{8}\alpha_M \omega \tan\theta_1 = \tfrac{1}{8} Fr\, N \cos^2\theta \tan\theta_1. \tag{6.4}$$

This is typically 3 times higher than the asymptotic result (5.14) for the resonant triads, which has been found to be in good agreement with the numerical computations. For instance:

for the primary mode (1,1), $s_q T_{BV} = 1.04\, Fr$, instead of $0.308\ Fr$ from (5.14);

for the primary mode (5,1), $s_q T_{BV} = 1.34\, Fr$, instead of $0.492\ Fr$ from (5.14).

Therefore, while the observed structure of the growing perturbation is quite in agreement with this idea of local parametric instability, the actual instability mechanism is less efficient.

This difference is not commented on by McEwan & Robinson (1975). We propose an interpretation based on the fact that the perturbation is a wave packet rather than an ideal plane wave. Therefore some energy must be radiated away from the central region of generation, towards regions where the wave coherence is destroyed by the combined advective and propagative effects. Since a plane wave does not fit the boundary conditions, unlike the standing waves (3.1), such a limitation is necessary.

The energy radiation depends on the perturbation wavelength, and we need first to understand what determines this important quantity. The band structures for different primary wave amplitudes are represented on figure 15: their length is always of the same order as the horizontal half-wavelength π/k of the primary wave, while the typical perturbation wavelength λ is proportional to the amplitude of the primary wave. These results can be understood by the following arguments. We have first to consider that the local parametric instability excites perturbations with natural frequencies ω_q spreading within the instability tongue defined by

$$\frac{\omega}{2} - s < \omega_q < \frac{\omega}{2} + s.$$

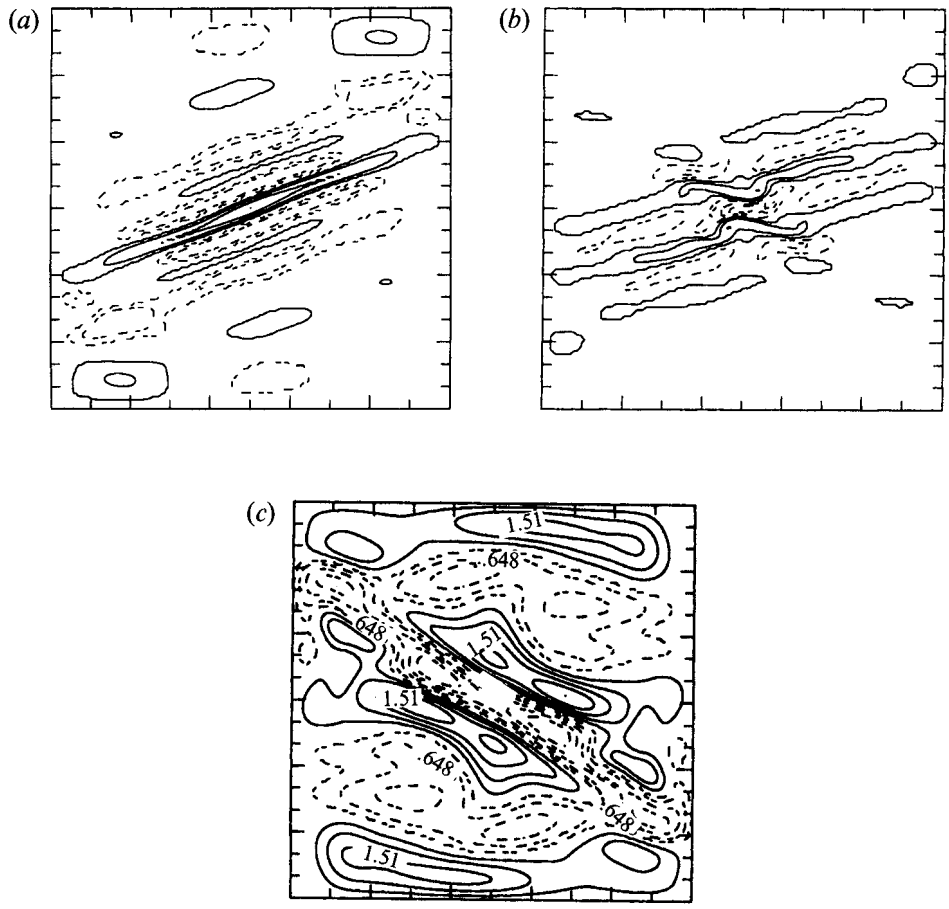

FIGURE 15. Vorticity bands obtained for three different primary wave amplitudes: (*a*) $a = 0.256$ (run V9), (*b*) $a = 0.328$ (run V8), (*c*) $a = 0.4$ (run V6), showing that the perturbation wavelength is roughly proportional to the primary wave amplitude ($k\lambda = 0.2Fr$).

This corresponds to a distribution of the angles θ_q for the excited wave vectors, with mean value θ_1 and typical width $\delta\theta_q$ given by differentiating the dispersion relationship (3.3)

$$N \sin\theta_1 \, \delta\theta_q = 2s$$

for small primary wave amplitudes. If the growing perturbation results from the superposition of waves with this distribution of wave vectors, a wave packet remains coherent over a length l if its mean wavelength is

$$\lambda = 2l \, \delta\theta_q = l \frac{4s}{N \sin\theta_1} \tag{6.5}$$

(indeed, the waves with angles in the range $[\theta_1 - \delta\theta_q/2, \theta_1 + \delta\theta_q/2]$, in phase at the wave packet centre, are shifted by $\lambda/4$ after a length $l/2$ such that interference is no longer constructive). This wavelength is proportional to the primary wave amplitude for a given length l.

The growth rate is well predicted by (5.14), instead of (6.4), and we write it in the form $s = (Fr/T_{BV})f(\theta)$, ($f(\theta) = 0.308$ for the mode (1, 1)), so that

$$\lambda = l\frac{2Fr}{\pi \sin\theta_1} f(\theta). \tag{6.6}$$

In order to estimate the length l, we need to consider a second condition for the perturbation coherence, associated with the transport by the primary wave. Indeed this advection tends to give any material line a sinusoidal shape, which can be assimilated as a straight line only in the central part. We expect the wave coherence to be lost at distances from the centre for which the shift with the central tangent straight line is of order $\lambda/2$. Using the displacement due to a linear primary wave (3.1) (we expand it at third order as a function of the distance from the centre), this condition leads to

$$(kl)^3 = \frac{k\lambda}{Fr\cos^3\theta} \frac{96}{7-(23/4)\cos^2\theta+\cos^4\theta}.$$

Combining this expression with (6.6), we get

$$(kl)^2 = \frac{1}{\cos^3\theta} \frac{96}{7-(23/4)\cos^2\theta+\cos^4\theta} \frac{f(\theta)}{\sin\theta_1} \frac{2}{\pi}$$

which indeed does not depend on the mode amplitude. For the mode (1,1), $\cos^2\theta = 1/2$, and this formula gives $l \sim \pi/k$ of the same order as the half-wavelength. Then (6.6) yields the perturbation wavelength, $kl = 0.2\,Fr$, in good agreement with numerical results.

The radiation of energy follows the group velocity, which is normal to the wavenumber vector for an internal wave, therefore along the wave crests. The value of this group velocity is

$$v_g = N \sin\theta_q / q$$

where q is the modulus of the wave vector $\boldsymbol{q}$ of the wave packet ($q = 2\pi/\lambda$), and the radiated energy flux is obtained by multiplying this velocity by the energy density. For a wave packet of length l along the crests and width d, the energy density is obtained by dividing the total perturbation energy E_q by the area ld. Since the energy flux is active over a typical width d on each side, the resulting rate of energy decay scales like $2v_gE_q/l$. Combining this loss with the production rate of energy by the parametric instability, twice the growth rate (6.4), we find a corrected growth rate

$$s = s_q - N\frac{\sin\theta_1}{l}\frac{\lambda}{2\pi} = FrN\left[\frac{\cos^2\theta\tan\theta_1}{8} - \frac{f(\theta)}{\pi^2}\right] \tag{6.7}$$

where λ has been estimated by (6.6). This reduced growth rate is thus proportional to the primary wave amplitude, as observed, but the numerical value is still too high ($s = 0.13\,Fr\,N$, i.e. $s\,T_{BV} = 0.84\,Fr$, for the mode (1,1)).

6.2. *Life time of the primary wave and breaking mechanisms*

The occurrence of wave breaking itself is not easy to specify in practice. We can consider the time for maximum energy decay. We can alternatively check when the Froude number (i.e. the vorticity in our computations) somewhere exceeds a threshold value greater than 1, indicating that some turbulence is produced, as discussed below. However these different criteria are found to be in agreement within a few primary wave periods, and a remarkable scaling law is observed, whatever the

chosen definition: for a given structure of the initial condition, the life time before breaking increases in proportion to the inverse square of the amplitude, as shown in figure 16. This is surprising, since the growth rate of the instability is proportional to Fr, so that a crude guess would give an inverse life time with Fr^{-1}.

We now propose a justification of this law, using the stability considerations of the previous section, but it is first useful to discuss the process of breaking itself. The instability becomes progressively very strong, and grows in typically one primary wave period, when the vorticity reaches a value of order N. This instability, described by Floquet theory, can then be physically interpreted in term of two basic mechanisms: (i) a shear instability occurring when the velocity of the perturbation is maximal, (ii) a convective instability associated with the local overhanging of the isodensity lines, occurring instead when the displacement is maximum. Thus both velocity shear and density overturning are expected to enhance parametric instabilities when the secondary wave exceeds a threshold amplitude. We here assume that for these two mechanisms the threshold values are given by the following criteria. Shear instability is expected when the Richardson number is smaller than 1/4 (e.g. Drazin & Reid 1981): $Ri = N^2/(\partial_y U)^2 < 1/4$, while convective instability is expected when the vertical density gradient becomes locally positive: $-N^2 + \partial_y \rho' > 0$. The influence of diffusion is specified by Thorpe (1994*a*), for a simple model of the density profile: comparisons with our computations indicate that diffusion effects do not significantly alter this condition of static instability. In fact, and because of the horizontal shear produced by the primary wave, convective instability is here unlikely to occur since the dynamics are restricted to a vertical plane (Deardorff 1965). Instead the wave seems to break through a shear instability, leading rapidly to fine-scale structures. We thus find that wave breaking occurs when the maximum vorticity reaches $2N$ (as given by the stability criterion above).

Therefore, the perturbation grows with vorticity amplitude

$$\zeta_q = \zeta_0(q) \exp(s_q t)$$

until breaking occurs for $\zeta_q \sim 2N$. This is then obtained at a time t_b such that

$$s_q t_b = \log(2N/\zeta_0(q))$$

and it is natural to suppose that this time should scale like the inverse of the growth rate, with Fr^{-1}, with only a weak logarithmic dependency on the initial perturbation. However, the amplitude of this initial perturbation must exponentially decrease with the wavenumber q. Indeed, as discussed in § 5.3, the wavenumber q is excited at typical order $n \sim q/k$ in the Froude number expansion, with a corresponding vorticity amplitude Fr^n; its logarithm scales like $-q/\log Fr^{-1}$: it is proportional to the wave number q. This fact is quite general and related to the analyticity of dynamical fields during the first oscillations (this is long before breaking); the spectrum of any analytical function must decay exponentially at large wavenumbers. Now the important point is that the wavenumber q of the growing perturbation scales like Fr^{-1} by (6.6), so that

$$t_b = cFr^{-2} \log(Fr^{-1}) T_{BV}$$

where the coefficient c depends only on the primary wave structure, but not on its amplitude. The observed law in Fr^{-2} is then explained, with a logarithmic correction, which would be difficult to check because of our limited range of wave amplitudes.

We have checked that the life time is indeed sensitive to the initial perturbation, as expected from the previous arguments, but it is dominantly controlled by the primary

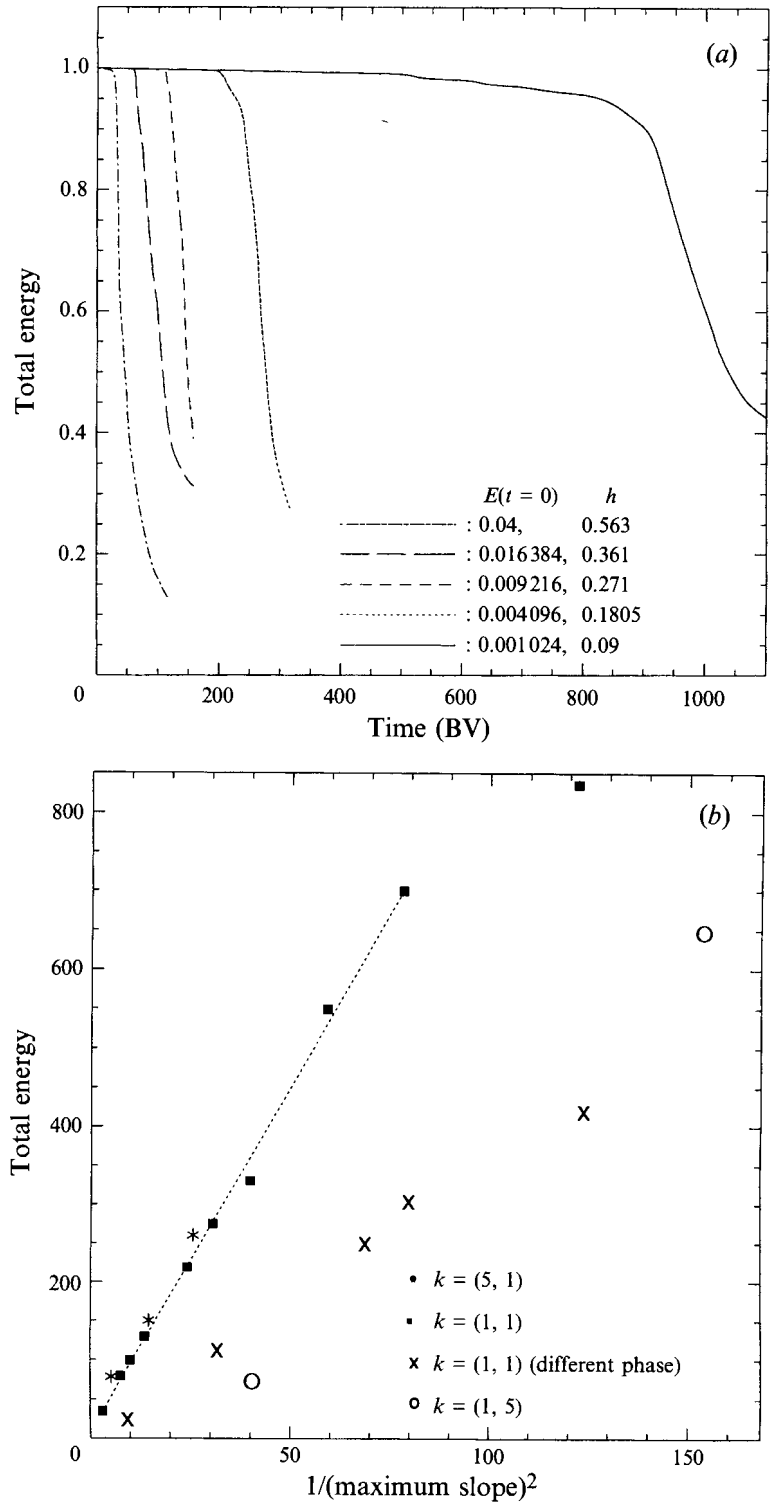

FIGURE 16. For caption see facing page.

wave amplitude. For instance, we have added a white noise of the form $W.f(x, y)$ on the vorticity field every 100 time steps (f is a random function with a uniform probability in the interval [-0.5,0.5]). When W is 0.8% of the maximum initial wave vorticity, the life time becomes 55 T_{BV} instead of 75 T_{BV} for the pure wave (with $a = 0.256$), and it reduces to 45 T_{BV} when the vorticity perturbation W is 8%.† Initiating the calculation with a pure density perturbation of a linear wave, plus its first-order perturbation, instead of a pure velocity (3.1), leads also to a somewhat shorter life time of 55 T_{BV}. Nevertheless, a dependency of the life time as Fr^{-2} is also obtained with this second class of initial condition (figure 16).

7. Conclusion

We conclude that the standing internal gravity wave eventually breaks, and this breaking is associated with energy dissipation, which becomes practically independent of viscosity for high Reynolds number (as shown in figure 8*b*): the breaking is controlled by inertial effects, although the eventual energy dissipation is due to viscosity and diffusion. This is analogous to the energy cascade in unstratified turbulence. Irreversible vertical transport of matter is also associated with breaking, and this has been studied by Bouruet-Aubertot (1994), as well as other statistical features of the decaying turbulent regime resulting from breaking. We have limited the present paper to the mechanisms of instability which lead to wave breaking, while the statistical aspects are reported by Bouruet-Aubertot *et al.* (1994).

The strong instability leading to wave breaking is preceded by a slow instability by resonant wave interactions. In the absence of dissipative effects, such instabilities always develop, whatever the primary wave amplitude (the growth rate is proportional to Fr for small primary wave amplitudes). This fact has already been recognized by various authors, and checked in laboratory experiments. In particular, the importance of the parametric subharmonic instability was emphasized. However, the structure and properties of the growing instability could not be fully analysed in laboratory experiments, due to difficulties of flow characterization and limited control of the initial conditions. The present numerical computations, performed with much higher spatial resolution than earlier studies on this subject, give a clear picture of the mechanisms leading to wave breaking. These computations provide good tests and illustrations of old theoretical conjectures, but they also reveal a remarkable organization of the unstable modes associated with nonlinear effects.

The initiation of wave breaking can be considered as a problem of instability of an ideal periodic standing wave of finite amplitude, approached using (3.4). If the spatial structure of such a nonlinear wave is not exactly realized in the initial condition (for instance with the linear wave approximation (3.1)), the small difference will be amplified by an instability process. For the case of standing waves, the linear stability

† Then a slight increase of the instability growth rate by 6% is observed in addition to the effect on the initial perturbation. Such an increase of the energy transfers in the background of internal wave fields has been described by Orlanski & Cerasoli (1980).

FIGURE 16. (*a*) Energy decay observed for different amplitudes of the initial wave, mode (1, 1). (*b*) Lifetime of the wave versus the square of the maximum slope $h = k_x{}^2 a/\omega$ of the primary wave iso-density lines; the linear fits are indicated, for an initial excitation in stream function (3.1) (dotted line), and for an initial excitation made of the linear wave density (3.2), with $\omega t = \pi/2$, plus the associated first-order density perturbation, given in (8) (solid line).

analysis has been done only in the limiting case of small primary wave amplitude (Fr much smaller than 1), which already provides a good approach to the more general case. Instability occurs through resonant triads given by diagrams like figure 10, further restricted by the condition of wave vector quantization. Instability occurs either through isolated triads, or along asymptotic branches of high wave vectors, for which the constraint of quantization is no more effective. For primary waves of fairly high frequencies (for instance $k = (5, 1)$ and $k = (1, 1)$), such asymptotic branches have the highest growth rate, so that many modes, with the same frequency equal to half the primary wave frequency, but very different wavelengths, can grow on equal bases according to linear stability analysis (this is true only when viscosity is sufficiently small so that the asymptotic branches are really reached before significant reduction of growth rate occurs by viscous damping). Therefore the selection of the unstable structure must occur through nonlinear effects. Generally such problems of mode selection through nonlinear effects occur with modes of similar scale: for instance in the control of instability patterns in the plane (like rolls, squares or hexagons). We are not aware of any study of this problem of nonlinear mode selection in the presence of a hierarchy of mode scales. The result of the numerical computations is that these modes organize in a coherent way to form remarkable band structures, as shown in figure 4. Such structure can be described as a plane wave packet, but its decomposition in terms of standing waves, which fit with the boundary conditions, involve many modes. The organization of all these growing modes into such a structure is probably related to the fact that nonlinear effects vanish in a plane wave: such a perturbation is allowed to grow without limitation, until it becomes strongly unstable. The wavelength of this secondary wave packet is roughly proportional to the primary wave amplitude. We propose a mechanism of selection of this wavelength involving local amplification of the wave packet by parametric instability, as described by McEwan & Robinson (1975), and a loss of energy by radiation away from the packet. The latter mechanism depends on the wavelength while the former does not.

For specific values of the primary wave frequency, instability can also grow through isolated resonant triad interactions. This is the case for the initial mode (1,1) which feeds the secondary modes (2,6) and (3,7). This perturbation grows by superposition with the band structure corresponding to the asymptotic branch. Each of these two perturbations oscillates with its own frequency, with nearly the same growth rate, and they significantly interact only as breaking is approached. As they grow in amplitude, such isolated triads can transfer energy to new triads as a secondary instability, and such a 'cascade' transfers energy to smaller and smaller scales, leading to steeper and steeper waves, until strongly nonlinear effects produce wave breaking. Such a scenario has been often conjectured, for instance in McEwan (1983). However in our calculations, the formation of the wave packet clearly dominates the vorticity fields, and therefore leads first to the conditions of strong nonlinearity. This wave packet corresponds to the 'traumata' described in laboratory experiments, and visualized in figure 6(a). The discussion of the role of these 'traumata' with respect to isolated triad interactions was often confusing in previous reports of laboratory experiments. Our numerical computations clearly show that the formation of these perturbations is the leading phenomenon in the initiation of wave breaking.

Notice however that this organized wave packet appears only when the asymptotic branch of parametric instability has the maximum growth rate (figure 11). This is true for a primary wave of fairly high frequency, but not for a low-frequency wave like the mode (1,5). Then isolated triads have a maximum growth rate (branch C in figure 10). Also secondary modes at higher frequency than the primary wave can be

resonantly excited (although not in the limit of small primary wave amplitude), and seem to dominate the approach of wave breaking in a typical run like in figure 9. These cases of low-frequency waves clearly need further investigations.

Finally the life time of the standing wave follows a remarkable law in Fr^{-2}, for a given initial wave structure (figure 16). The life time is defined as the time after which the energy decay is maximum, providing an evaluation of the instant of breaking. This law can be reconciled with the growth rate in Fr, by considering the amplitude of the initial perturbation, together with the scaling law in Fr^{-1} for the perturbation wavenumber q. As expected from this argument, the life time depends on the presence of small perturbations, but not to a very large extent. Therefore our calculations of the life time should give quite realistic values even in a real standing wave subjected to perturbations.

The possibility of applying these results to the breaking in more general internal wave fields deserves further investigations. The presence of a periodic primary wave, rather than a more complex wave field, is probably essential to feed the secondary wave packet by parametric instability. Propagating waves in an infinite domain, or in a horizontal channel (with vertical confinement) could probably display similar properties. Since periodic internal waves are produced by the interaction of oceanic currents with bottom topography, such a formation of bands may lead to observable features in the density field and positions of mixing events. Applications to other waves with similar dispersive properties, in particular inertial waves of rotating fluids, should also be considered.

We thank S. A. Thorpe for pertinent comments on this work. The program and advice on time-frequency analysis have been kindly provided by P. Flandrin and F. Auger. This work has been supported by a DRET contract (no. 90/1650/A000) and by a DRET-CNRS grant. Part of the calculations have been performed on the Cray 2 of CCVR, thanks to computing time allocated by CNRS (Dept of Physical and Mathematical Sciences) and by the Ministry of Education (DRED Matter Science Dept).

REFERENCES

AUGER, F. & FLANDRIN, P. 1994 Generalization of the reassignment method to all bilinear time-frequency and time scale representations. In *Proc. of ICASSP'94 (Int. Conf. on Acoustics, Speech and Signal Processing), 19–22 April 1994, Adelaide Convention Center, Adelaide, South Australia*, Vol. IV, pp. 317–320.

BARTOLONI, A., BATTISTA C., CABASINO, S., PAOLUCCI, P. S., PECH, J., SARNO, R., TODESCO, G. M., TORELLI, M., TROSS, W. & VICINI, P. 1993 LBE simulations of Rayleigh-Benard convection on the APE100 parallel processor. *J. Mod. Phys.* C **4**, 993.

BENDER, C. M. & ORSZAG, S. A. 1978 *Advanced Mathematical Methods for Scientists and Engineers.* McGraw-Hill.

BENIELLI, D. & SOMMERIA, J. 1994 Excitation of internal waves and stratified turbulence by parametric instability. Submitted to *Dyn. Atmos. Oceans* (*Special Issue 4th Intl Symp. on Stratified Flows* (ed. E. J. Hopfinger and B. Voisin)).

BOURUET-AUBERTOT, P. 1994 Instabilités et déferlement d'ondes internes de gravité. Thèse de doctorat, Université de Lyon.

BOURUET-AUBERTOT, P., SOMMERIA, J. & STAQUET, C. 1994 Stratified turbulence produced by internal wave breaking. Submitted to *Dyn. Atmos. Oceans* (*Special Issue 4th Intl Symp. on Stratified Flows* (ed. E. J. Hopfinger & B. Voisin)).

BRACHET, M. E. & MENEGUZZI, M. & POLITANO, H. & SULEM, P. L. 1988 The dynamics of freely decaying two-dimensional turbulence. *J. Fluid Mech.* **194**, 333–349.

CANUTO, C., HUSSAINI, M. Y., QUATERONI, A. & ZANG, T. A. 1988 *Spectral Methods in Fluid Dynamics.* Springer.

CHRISTIE, S. L. & DOMARADZKI, J. A. 1992 Numerical evidence for nonuniversality of the soft/hard turbulence classification for thermal convection. *Phys. Fluids* A **5(2)** 412–421.

DAVIS, R. E. & ACRIVOS, A. 1967 The stability of oscillatory internal waves. *J. Fluid Mech.* **30**, 723–736.

DEARDORFF, J. W. 1965. Gravitational instability between horizontal plates with shear. *Phys. Fluids,* **8**, 1027–1030.

DELUCA, E. E., WERNE, J., ROSNER, R. & CATTANEO, F. 1990 Numerical simulations of soft and hard turbulence: preliminary results for two-dimensional convection. *Phys. Rev. Lett.* **64**, 2370–2373.

DRAZIN, P. G. 1977 On the instability of an internal gravity wave. *Proc. R. Soc. Lond.* A **356**, 411–432.

DRAZIN, P. G. & REID, W. H. 1981. *Hydrodynamic Stability*, Cambridge University Press.

HASSELMANN, K. 1962*a* On the non-linear energy transfer in a gravity wave spectrum, Part 1. *J. Fluid Mech.* **12**, 481–500.

HASSELMANN, K. 1962*b* On the non-linear energy transfer in a gravity wave spectrum. Part 2. *J. Fluid Mech.* **15**, 273–281.

HASSELMANN, K. 1967 A criterion for nonlinear wave stability. *J. Fluid Mech.* **30**, 737–739.

KLOSTERMEYER, J. 1982 On parametric instabilities of finite-amplitude internal gravity waves. *J. Fluid Mech.* **119**, 367–377.

KLOSTERMEYER, J. 1983 Parametric instability of internal gravity waves in Boussinesq fluids with large Reynolds numbers. *Geophys. Astrophys. Fluid Dyn.* **26**, 85–105.

KLOSTERMEYER, J. 1990 On the role of parametric instability of internal gravity waves in atmospheric radar observations. *Radio Sci.* **25**, 983–985.

KLOSTERMEYER, J. 1991 Two and three-dimensional parametric instabilities in finite amplitude internal gravity waves. *Geophys. Astrophys. Fluid Dyn.* **61**, 1.

KRAICHNAN, R. H. & MONTGOMERY, D. 1980 Two-dimensional turbulence, *Rep. Prog. Phys.* **43**, 547–617.

KUNZE, E. & WILLIAMS, A. J. & BRISCOE, M.G. 1990 Observations of shear and vertical stability from a neutrally buoyant float. *J. Geophys. Res.* **95**, 127–141.

MCEWAN, A. D. 1971 Degeneration of resonantly-excited standing internal gravity waves, *J. Fluid Mech.* **50**, 431–448.

MCEWAN, A. D. 1983 Internal mixing in stratified fluids. *J. Fluid Mech.* **128**, 59–80.

MCEWAN, A. D., MANDER, D. W. & SMITH, R. K. 1972 Forced resonant second-order interactions between damped internal waves. *J. Fluid Mech.* **55**, 589–608.

MCEWAN, A. D. & PLUMB, R. A. 1977 Off-resonant amplification of finite internal wave packets. *Dyn. Atmos. Oceans,* **2**, 83–105.

MCEWAN, A. D. & ROBINSON, R. M. 1975 Parametric instability of internal gravity waves. *J. Fluid Mech.* **67**, 667–687.

MIED, R. P. 1976 The occurrence of parametric instabilities in finite-amplitude internal gravity waves. *J. Fluid Mech.* **78**, 763–784.

MULLER, P., HOLLOWAY, G., HENYEY, F. & POMPHREY, N. 1986 Non linear interactions among internal gravity waves. *Rev. Geophys.* **24**, 493–536.

ORLANSKI, I. 1972 On the breaking of standing internal waves. *J. Fluid Mech.* **54**, 577–598.

ORLANSKI, I. & BRYAN, K. 1969 Formation of the thermocline step structure by large-amplitude internal gravity waves. *J. Geophys. Res.* **74**, 6975–6983.

ORLANSKI, I. & CERASOLI, C. P. 1980 Resonant and non-resonant wave-wave interactions for internal gravity waves. *Marine Turbulence, Proc. 11th Int. Colloquium on Ocean Hydrodynamics,* pp. 65–100.

ORLANSKI, I. & ROSS, B. B. 1973 Numerical simulations of the generation and breaking of internal gravity waves. *J. Geophys. Res.* **78**, 8808–8826.

PHILLIPS, O. M. 1960 On the dynamics of unsteady gravity waves of finite amplitude. Part 1. *J. Fluid Mech.* **9**, 193–217.

PHILLIPS, O. M. 1961 On the dynamics of unsteady gravity waves of finite amplitude. Part 2. *J. Fluid Mech.* **11**, 143–155.

SEKERZH-ZEN'COVICH, S. YA. 1983 Parametric resonance in a stratified liquid undergoing vertical vibrations. *Sov. Phys. Dokl.* **28**, 445–446.

STAQUET, C. 1991 Influence of a shear on a stably-stratified flow. In *Turbulence and Coherent Structures* (ed. O. Metais and M. Lesieur). Kluwer.

TAYLOR, J. R. 1992 The energetics of breaking events in a resonantly forced internal wave field. *J. Fluid Mech.* **239**, 309–340.

THORPE, S. A. 1968 On standing internal gravity waves of finite amplitude. *J. Fluid Mech.* **32**, 489–528.

THORPE, S. A. 1994*a* The stability of statically unstable layers. *J. Fluid Mech.* **260**, 315–331.

THORPE, S. A. 1994*b* Statically unstable layers produced by overturning internal gravity waves. *J. Fluid Mech.* **260**, 333–350.

THORPE, S. A. 1994*c* Observations of parametric instability and breaking waves in an oscillating tilted tube. *J. Fluid Mech.* **261**, 33–45

WINTERS, K. B. & D'ASARO, E. A. 1989 Two-dimensional instability of finite amplitude internal gravity wave packets near a critical level. *J. Geophys. Res.* **94**, 12709–12719.

WINTERS, K. B. & RILEY, J. J. 1992. Instability of internal waves near a critical level. *Dyn. Atmos. Oceans* **16**, 249–278.